International Journal of Nanomedicine

Dovepress

Open Access Full Text Article

ORIGINAL RESEARCH

Enhancing Photothermal Therapy for Antibiofilm Wound Healing: Insights from Graphene Oxide-Cranberry Nanosheet Loaded Hydrogel in vitro, in silico, and in vivo Evaluation

Sammar Fathy Elhabal[1], Saeed AS Al-Zuhairy[2], Mohamed El-Nabarawi[3], Mohamed Fathi Mohamed Elrefai[4,5], Mai S Shoela[6], Sandra Hababeh[7], Jakline Nelson[8], Mohamed A Abdel Khalek[9], Marwa Fady[10,11], Nahla A Elzohairy[11,12], Mariam E Amin[13], Gehad M Khamis[6], Amira Rizk[14], Sara Mohamed Ahmed[15], Ahmed A El-Rashedy[16], Mohamed Mohany[17], Abdulaziz S Al-Roujayee[18], Ahmed Mohsen Faheem[19], Amr Amin[20]

[1]Department of Pharmaceutics and Industrial Pharmacy, Faculty of Pharmacy, Modern University for Technology and Information (MTI), Mokattam, Cairo, Egypt; [2]Department of Pharmacy, Kut University College, Kut, Wasit, Iraq; [3]Department of Pharmaceutics and Industrial Pharmacy, Faculty of Pharmacy, Cairo University, Cairo, Egypt; [4]Department of Anatomy, physiology and Biochemistry, Faculty of Medicine, the Hashemite University, Zarqa, Jordan; [5]Department of Anatomy and Embryology, Faculty of Medicine, Ain Shams University, Cairo, Egypt; [6]Department of Clinical Pharmacology, Faculty of Medicine, Alexandria University, Alexandria, Egypt; [7]Department of Pharmaceutics, College of Pharmacy, King Saud University, Riyadh, Saudi Arabia; [8]Department of Microbiology and Immunology, Faculty of Pharmacy, Nahda University, Beni-Suef, Egypt; [9]Institute of Nanoscience and Nanotechnology, Kafrelsheikh University, Kafrelsheikh, 33516, Egypt; [10]Zagazig University Hospitals, Infection Control Unit, Zagazig, 44519, Egypt; [11]Modern University for Technology & Information, Department of Microbiology and Immunology, Pharmacy College., Cairo Governorat, Egypt; [12]Air Force Specialized Hospital, Cairo, Egypt; [13]Microbiology and Immunology Department, Faculty of Pharmacy, Suez Canal University, Ismailia, Egypt; [14]Food Science and technology, Department Faculty of Agricultural, Tanta University, Tanta, Egypt; [15]Department of Pharmaceutics, College of Pharmaceutical Sciences and Drug Manufacturing, Misr University for Science and Technology, Giza, 12585, Egypt; [16]Chemistry of Natural and Microbial Products Department, National Research Center (NRC), Giza, Egypt; [17]Department of Pharmacology and Toxicology, College of Pharmacy, King Saud University, Riyadh, Saudi Arabia; [18]Department of Dermatology and Venereology, College of Medicine, Al Imam Mohammad Ibn Saud Islamic University, Riyadh, Saudi Arabia; [19]Department of Medical Biochemistry and Molecular Biology, Faculty of Medicine, Mansoura University, Mansoura, Egypt; [20]College of Medicine, Sharjah University, Sharjah, United Arab Emirates

Correspondence: Sammar Fathy Elhabal; Amr Amin, Email sammar_fathy2007@yahoo.com, sammar.fathy@pharm.mti.edu.eg; a.amin@sharjah.ac.ae

Background: Diabetic foot ulcers present a formidable challenge due to colonization by biofilm-forming microorganisms, heightened oxidative stress, and continuous wound maceration caused by excessive exudation.

Methods: To address these issues, we developed a robust, stretchable, electro-conductive, self-healing, antioxidant, and antibiofilm hydrogel. This hydrogel was synthesized through the crosslinking of polyvinyl alcohol (PVA) and chitosan (CH) with boric acid. To enhance its antimicrobial efficacy, graphene oxide (GO), produced via electrochemical exfoliation in a zinc ion-based electrolyte medium, was incorporated. For optimal antibiofilm performance, GO was functionalized with cranberry (CR) phenolic extracts, forming a graphene oxide-cranberry nanohybrid (GO-CR).

Results: The incorporation of GO-CR into the hydrogel significantly improved its stretchability (280% for PVA/CH/GO-CR compared to 200% for PVA/CH). Additionally, the hydrogel demonstrated efficient photothermal conversion under near-infrared (NIR) light, enabling dynamic exudate removal, which is expected to minimize retained exudate between the wound and the dressing, reducing the risk of wound maceration. The hydrogel effectively reduced levels of lipopolysaccharide (LPS)-induced skin inflammation markers, significantly lowering the expression of NLRP3, TNF-α, IL-6, and IL-1β by 39.2%, 31.9%, 41%, and 52.3%, respectively. Histopathological and immunohistochemical analyses further confirmed reduced inflammation and enhanced wound healing.

Conclusion: The PVA/CH/GO-CR hydrogel exhibits multifunctional properties that enhance wound healing ulcers. Its superior mechanical, antibacterial, and anti-inflammatory properties and ability to promote angiogenesis make it a promising candidate for effective wound management in diabetic patients.

Keywords: antibiofilm, cranberry extract, electro conductive hydrogel, graphene oxide, nanocomposite, photothermal conversion, self-healing, wound healing

Received: 12 August 2024
Accepted: 12 November 2024
Published: 3 December 2024

Graphical Abstract

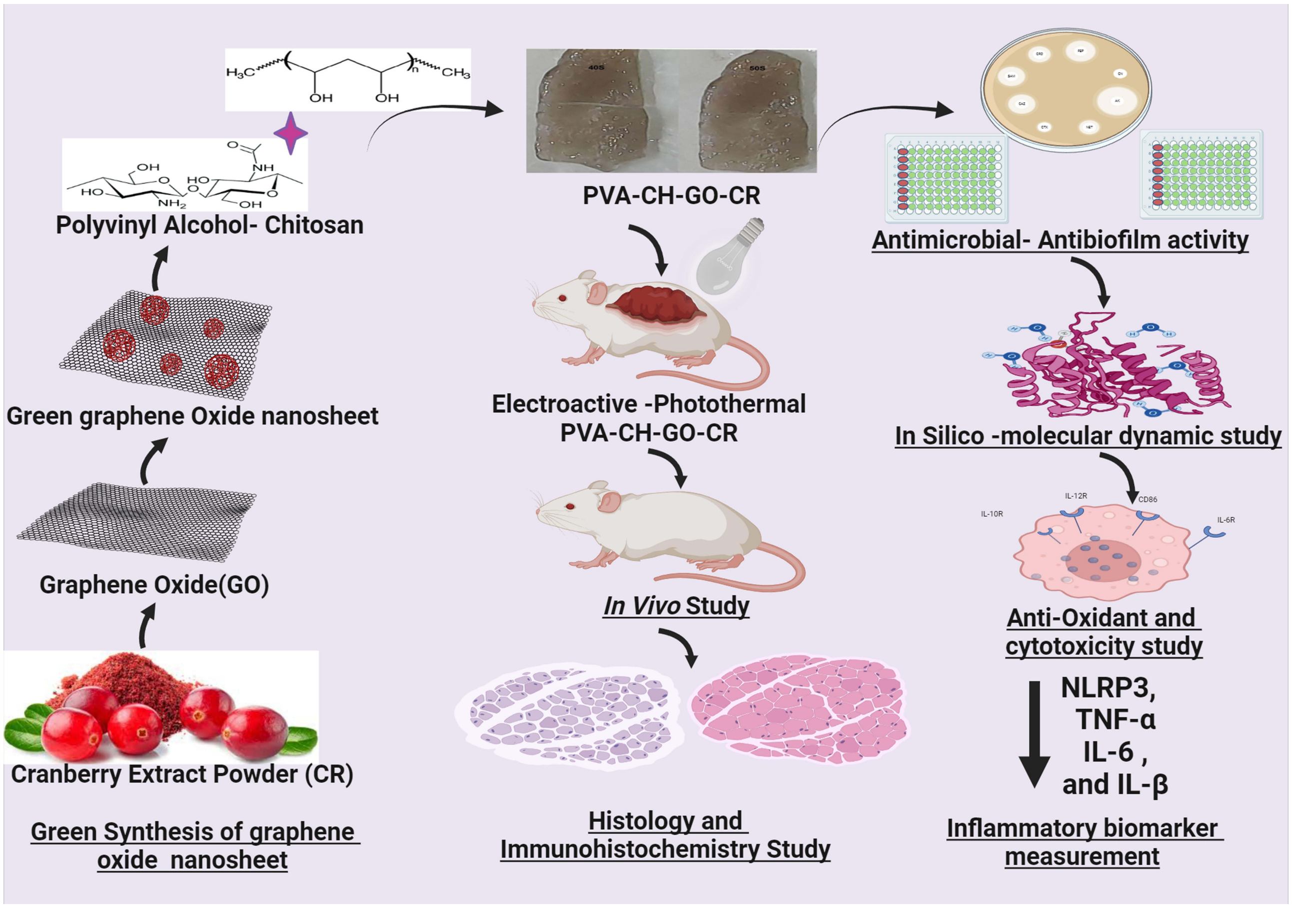

Introduction

The skin, the body's largest organ, serves as its outermost protective covering, shielding against external interference.[1] Wounds arise primarily from skin damage induced by various factors, including thermal, physical, chemical, immunological, and microbiological agents. Any skin injury creates a gateway for bacteria to infiltrate the wound, leading to potential infection.[2] The wound healing process encompasses four stages: hemostasis, inflammation, proliferation, and remodeling. Different types of wounds and injuries to the skin, such as burns, abrasions, bites, cuts, scrapes, scratches, and surgical incisions, usually result from blunt or penetrating trauma. They tend to heal with minimal complications and within a relatively short period.[3] Diabetes and hypertension are underlying disorders that impede the healing process by extending the inflammatory phase, increasing the risk of infection, encouraging the growth of bacterial biofilms resistant to antibiotics, and preventing dermal and/or epidermal cell responses. Diabetic complications over the long term, often associated with neuropathy, vascular impairment, and hyperglycemia, can give rise to diabetic ulcers.[4] Several natural extracts have demonstrated wound-healing potential among individuals with diabetes. Some of these extracts, including Cranberry powder (CR), *Althaea officinalis* (Marshmallow), *Aloe vera*, Honey, Turmeric, Curcumin, Green Tea, Ginseng, Chamomile, and *Ginkgo biloba*, have been studied for their efficacy in diabetic wound healing.[1,5]

Cranberries (*Vaccinium macrocarpon*) are rich in polyphenols, triterpenoids, hydroxycinnamic and other phenolic acids, catechins, and three classes of flavonoids (flavanols, anthocyanins, and proanthocyanidins). These compounds act as potent antioxidants, minimizing cellular damage and scavenging free radicals.[6] The diverse array of Proanthocyanidins (PACs) found in cranberries may contribute to their significant bioactivity against urinary tract infections (UTIs).

Cranberry extracts have shown promising potential in wound healing, yielding several beneficial outcomes such as accelerated wound contraction, increased vascularization, re-epithelialization, collagen production, reduced oxidative stress and inflammation, and antibacterial properties at the wound site.[7] The challenging nature of wound healing prompted the exploration of various biomaterials like hydrogels, nanofibers, microneedles, and hydrocolloid membranes to enhance wound recovery.[8] Nanotechnology has witnessed significant growth, with nanoparticles increasingly utilized in diverse medical applications, including drug delivery, biosensors, regenerative medicine, cancer phototherapy, tissue regeneration, bioimaging, bioimplants, and wound healing. Accordingly, nanoparticles are employed in wound healing to expedite healing and prevent infection infiltration into the wound site.[9]

Polyvinyl alcohol (PVA) is widely used for its fiber/film-forming ability, chemical and mechanical resilience, non-carcinogenicity, barrier properties, and high water-swelling capacity; for wound-dressing, PVA must be crosslinked, which helps it swell and retain water but prevents it from dissolving. Since PVA absorbs well, it has been utilized to treat many exudative lesions.[10] Chitosan and PVA can be used alone to make hydrogels but utilizing them together reduces their drawbacks. A biocompatible and non-toxic hydrogel, PVA/Chitosan could treat burn wounds or regenerate bone.[11]

Chitosan (Ch) has garnered attention in burn dressings because it can effectively adsorb bacterial toxins and mitigate unpleasant odours. Furthermore, its porous structure facilitates enhanced drug loading with antimicrobial agents. Ch is inherently water-soluble and does not necessitate organic solvents due to the presence of hydroxyl and amine groups. However, its water solubility can be enhanced by incorporating additional substances.[1] As a non-toxic biopolymer, Ch exhibits excellent adherence to mucosal surfaces. Ch possesses favorable attributes such as a positive charge, biocompatibility, and biodegradability.[5,12] It shows minimal antimicrobial and immunogenic properties. Ch offers high drug loading capacity and controlled release by leveraging its chemical activity and expansive specific surface area. Its mucoadhesive properties facilitate the development of bio-adhesive drug carrier systems capable of adhering to the skin and intestinal mucosa.[13,14] Consequently, Ch emerges as an ideal candidate for various drug delivery systems targeting cancer, antibacterial, antiulcer, and anti-inflammatory treatments.[15]

Graphene oxide (GO) is utilized more in biomedicine than graphene owing to its superior physical and chemical properties.[16] In recent years, biomaterials, drug delivery systems, and disease diagnostics have extensively employed GO and its composite nanomaterials. GO, characterized by its large specific surface area and multiple functional groups such as hydroxyl, carboxyl, and epoxy groups, exhibits efficient drug transport capabilities, making it a versatile nanomaterial with numerous biological applications. GO nanosheets can absorb biomolecules containing these functional groups and are well recognized as a groundbreaking tool in the fight against drug-resistant bacteria.[17] However, several studies have reported its inefficacy, casting doubt on its antibacterial properties. GO can function individually against bacteria or as a linking agent to develop a novel antibacterial weapon. Nonetheless, utilizing and synthesizing GO from metal nanoparticles could potentially harm organisms and contribute to environmental pollution. Conventional approaches for producing involve ultrasonically breaking down natural graphite powder, introducing oxygen-containing groups between graphite layers and subjecting it to multiple rounds of oxidation using potent oxidants and acids.[18]

In this study, a novel electroconductive, self-healing hydrogel was developed by crosslinking PVA/CH with boric acid. The hydrogel's morphology, physicochemical properties, and mechanical characteristics were thoroughly evaluated. Loaded with a graphene oxide-cranberry complex (GO-CR), the hydrogel underwent antioxidant, anti-inflammatory, and antibiofilm assessments. Its photothermal conversion under light exposure and the subsequent effect on water evaporation were also examined. The hydrogel's efficacy, along with its components, was investigated through a combination of in vitro, in vivo experiments, histological evaluations, immunohistochemistry analyses, and in silico studies.

Materials and Methods

Materials

Zn $(NO_3)_2.6H_2O$ was obtained from LOBA CHEM India. PVA (MW 80000), Chitosan (CH), streptozotocin (STZ) and were purchased from Fluka-Sigma-Aldrich, St. Louis, MO, USA. Dry Cranberry was purchased from EMA Pharm Egypt.

Methods

The hydroalcoholic extract of cranberry was prepared by macerating dried cranberry grinded fruit powder in a mixture of ethanol and water (70:30 v/v) at room temperature for 72 hours. The resulting extract was filtered and concentrated using a rotary evaporator under reduced pressure to remove the solvent. The concentrated extract was then freeze-dried to obtain a fine cranberry powder, which was stored in an airtight container at −20°C until further use, this powder was utilized in subsequent experiments.[19]

High-Performance Liquid Chromatography (HPLC-UV) Analysis of Phenolic Compounds in Cranberry (Cr)

Cranberry powder was tested using HPLC, which separates, identifies, and quantifies sample components. The study analyzed cranberry powder's primary flavonoids and phenolic acids using phenolic and flavonoid standards. HPLC analysis using an Agilent 1260 series system with a Zorbax Eclipse Plus C8 column (4.6 mm × 250 mm, 5 µm particle size). The mobile phases were water (A) and 0.05% trifluoroacetic acid in acetonitrile (B) with 0.9 mL/min linear gradient elution. Gradient elution began with 82% A at 0 minutes, held for 1 minute, then increased to 60% A over 18 minutes and returned to 82% over 24 minutes. A 280 nm multi-wavelength detector received five microliters of sample solution for detection. The column temperature was 40°C throughout the analysis. Phenolic compound retention periods and UV spectra were compared to reference compounds for identification. Each component was quantified in milligrams per gram of crude extract. Gallic acid, syringic acid, rosmarinic acid, apigenin, benzoic acid, and chlorogenic acid were investigated in cranberry powder.[20,21]

Electrochemical Exfoliation of GO

The electrolyte was 20%W/V NaCl and 7%Zn $(NO3)2.6H2O$. This solution was placed in a 20-mL glass bottle. The two graphite electrodes were then immersed in this solution and powered by 17VDC for 2h. Electrochemical exfoliation of the graphite rod created a black suspension. The dark residue was removed, and the supernatant was decanted and dried to isolate GO nanoflakes. GO-CR was made by dispersing 100mg of GO in 20 mL of 3% cranberry extract. The suspension dried after 3h of stirring.[16]

Hydrogel Formation

The PVA/CH/GO-CR hydrogel was prepared by homogenizing 8mL of 10%PVA with 2mL of 5%CH. After that, 100mg of GO-CR was dispersed in the PVA-CH by sonication for 10min. The crosslinking of the hydrogel was performed by pipetting 5mL (drop by drop) of 5% w/v of boric acid over PVA/CH/GO-CR solution.[22]

Characterization of GO-CR and Hydrogel

GO-CR and hydrogel morphology were examined using Transmission and Field Emission Scanning Electron Microscopy (FEG, Thermo Scientific NL, Quattro S.[23] FTIR studies were performed using a JASCO Fourier Transform Infrared Spectrometer (AUP1200343, Japan).[24,25] A longitudinal incision in the hydrogel was made to test its self-healing capabilities and the time it took to heal. A piece of hydrogel was connected to a 3V battery and LED circuit to measure its electric conductivity. Lloyd Instruments LR10 K with a 1 kN load cell and 2 mm/min crosshead speed measured the hydrogel's mechanical characteristics with samples were 2 cm × 10 cm.[26] The photothermal conversion efficacy of PVA/CH and PVA/CH/GO-CR was measured by putting 2 × 3cm hydrogels on glass slides and subjecting them to a 10W incandescent lamp. Temporal temperature rise was measured with an IR thermometer. The photothermal-induced fluid loss was measured by exposing accurately weighted hydrogel pieces to the incandescent lamp for different time intervals and weighing them again, the following calculation calculated weight loss.[14]

$$\text{Weight loss}(\%)=\frac{(\text{Initial weight} - \text{weight after light exposure})\times 100}{\text{Initial weight}}$$

Assay for Antioxidant Activity

Two millilitres of CR, GO-CR, PVA/CH/GO-CR hydrogel, and 0.1 mM DPPH solution were combined in methanol for 40 minutes.[27] The positive control sample for antioxidant activity was ascorbic acid (50 mg/20 mL MeOH, 0.008 mol). Spectrophotometry measured absorbance between 200 and 800 nm using methanol as a blank. The liquid was stirred for 45 minutes at 25 °C in an amber glass bottle.[28] Spectrophotometry assessed violet colour absorbance at 200–800 nm, and the antioxidant activity percentage was computed using the following equation:

$$\%\frac{\text{Antioxidant 1}}{\text{Antioxidant 2}}\times \text{ radical scavenging assay} = \frac{(\text{A0} - \text{A1})}{\text{A0}}\times 100$$

where A0 is the blank absorbance sample, and A1 is the absorbance of PVA/CH/GO-CR hydrogel.

Antimicrobial Assay

Bacterial Strains

The hydrogels CR, GO-CR, and PVA/CH/GO-CR were tested against resistant *Staphylococcus epidermidis* ATCC25922, *Klebsiella pneumonia* ATCC43816, *Pseudomonas aeruginosa* ATCC27853, and *E. coli* ATCC8739 in the Molecular laboratory at Nahda University Beni-Suef, Egypt.

Antibacterial Assay and Sensitivity

The inoculum, 100 microliters, or 10^7 CFU/mL, was combined with 20 mL of warm, melted BHA. The mixture was then transferred into the plate using a metal cup with a 6 mm diameter. Following the BHA's solidification, the metal cups were removed, 100 µL of each cranberry powder was put into the well for 24 hours, and the plate was incubated at 37°C. Each plant extract's antibacterial activity was assessed by measuring the inhibitory zone's diameter in millimetres.[29] Serially diluted cranberry powder, GO-CR, and PVA/CH/GO-CR hydrogel were incubated at 37°C for 24 hours. Microbial turbidity and broth recovery were used to determine MIC. The disc filter paper was submerged in 50 µL of each cranberry powder for 30 minutes to measure sensitivity and dried at room temperature. Recovery bacteria were put into plates and cultured for 24 hours to determine the inhibition zone.[30] The Clinical and Laboratory Standards Institute's (CLSI) recommended procedures for minimum inhibitory concentration (MIC) and minimum bactericidal concentration (MBC) were followed. In short, each extract's 10% stock solution was diluted twice serially in the brain-heart infusion broth (BHI) to get concentrations ranging from 0.02 to 25 mg/mL in 96-well microtiter plates with a total capacity of 100 mL each well. Each well was filled with 100 mL of each tested strain at a final concentration of 10^6 CFU/mL, and the wells were then appropriately incubated at 37 °C. The medium, 0.1% (w/v) CHX, and 10% DMSO were the non-treated, positive, and negative controls, respectively.

Antibiofilm Assay and Crystal Violet Staining (CVS) Assay

The microtiter plate 96 wells were divided into four strains mixed with serially diluted cranberry powder, GO-CR, and PVA/CH/GO-CR, and the last well was negative control. After the incubation period of 24 hours, the wells were gently emptied, and the plates were cleaned with a phosphate buffer with pH 7.2 at least three times after, as previously mentioned, to eliminate any loose or detached cells. After air drying, the plates were baked for 45 minutes at 60°C. Next, for 15–20 minutes, 150 µL of 96% methanol was applied to each well to fix the adhering cells.[31] After emptying the plates, the adherent cells were stained for 20 minutes at room temperature using 100 µL of 0.1% crystal violet solution. The plates were washed with water at least five times to remove any remaining discoloration. Next, the biofilm biomass was assessed semi-quantitatively using 150 µL of 100% ethanol to resolubilize the crystal violet dye attached to the adhering cells. The absorbance of the plates was read at 620 nm using a microplate reader (EpochTM Microplate Spectrophotometer) after careful and gentle shaking.[32] The mean absorbance (OD620 nm) of the sample was determined, and results were expressed as percentage inhibition using the equation Percentage of inhibition:

$$(\text{Control OD} - (\text{Sample OD}/\text{Control OD}))\times 100.$$

where Control OD is the absorbance of negative control, and Sample OD is the absorbance of the test sample.

In silico Study

System Preparation and Molecular Docking

UCSF Chimaera and Protein Data Bank prepared the three-dimensional structures of the receptor proteins for tumor necrosis factor-alpha with 6.7-dimethyl-3-[(methyl{2-[methyl({1-[3-(trifluoromethyl)phenyl]-1h-indol-3-yl}methyl) amino]ethyl}amino)methyl]-4h-chromen-4-one inhibitor (PDB ID: 2AZ5)([33]), epimerase N-acetylmannosamine-6-phosphate 2-epimerase (NanE) (PDB ID: 6VVA), and VEGF in complex with domain 2 of the flt-1 (PDB ID: 1FIT). PROPKA optimized pH to 7.5. The retrieved 2D structure was drawn in ChemBioDraw Ultra 12.1.[34] Avogadro software used the steepest descent and MMFF94 force field to reduce energy in the 2D construction. Before docking, UCSF chimera removed hydrogen atoms.[35]

Molecular Docking

Docking calculations were done using AutoDock Vina (9), and Gasteiger partial charges were assigned. AutoDock atom types were defined using MGL tools' AutoDock GUI. −19.4425, 69.9565, 34.2077 for 2AZ5; 102.405, 87.3446, 192.941 for 6VVA; 16.5532, 1.87971, 4.29795 for 1FIT were AutoDock Vina grid Centre coordinates. In all cases, the search space was 20 Å × 20 Å × 20 Å with an exhaustive score of 8. Lamarckian genetics created docked conformations in descending order based on docking energy.[4]

Molecular Dynamic (MD) Simulations

MD simulations allow researchers to study biological system atom and molecule mobility in ways that are difficult otherwise.[36] This simulation illuminates biological system dynamics, including molecule interaction and conformational changes. All MD simulations employed GPU PMEMD on AMBER 18. Each chemical's partial atomic charge was computed using ANTECHAMBER's GAFF. The AMBER 18 Leap module solved systems in an orthorhombic box of TIP3P water molecules within 10 Å of any edge. The Leap module neutralized each solution with Na+ and Cl-. Each system was initially minimized with a 500 kcal/mol constraint potential for 2000 steps and then fully minimized with a 1000-step conjugate gradient approach without constraints.[37]

In the MD simulation, each system was heated from 0K to 300K over 500 ps to guarantee identical atoms and volume. The solutes were contained in a 10 kcal/mol potential harmonic and a 1 ps collision frequency. For 500 ps, each system was heated to 300K to adapt. An isobaric-isothermal (NPT) ensemble was simulated in every production simulation, with the Berendsen barostat keeping both the atomic count and pressure constant at 1 bar. Each system was MD-simulated for 200 ns. Every simulation had atoms of hydrogen bonds restricted by SHAKE. An SPFP precision model and 2fs steps were used in each simulation. A randomized seeding, 1 bar pressure, 2 ps pressure-coupling constant, 300 K temperature, and 1 ps Langevin thermostat collision frequency were all employed in the simulations using an isobaric-isothermal ensemble (NPT).[38]

Post-MD Analysis

The CPPTRAJ[39] module of the AMBER18 suite was used to analyze the trajectories after they were saved every 1 ps from the MD simulations. All graphs and visualizations were made using Chimaera) and Origin, a data analysis tool.[40]

Thermodynamic Calculation

Calculations of ligand-binding affinity are improved by the Poisson-Boltzmann, generalized Born, and surface area continuum solvation (MM/PBSA and MM/GBSA) methods.[41,42] MM/GBSA and MM/PBSA Protein-Ligand complex molecular simulations yield realistic statistical-mechanical binding free energy in each force field. Average binding free energy from 200 ns trajectory images collected in 2000. The binding free energy (ΔG) variations for complex, ligand and receptor molecular species are estimated in the accompanying graphic:[43]

$$\Delta G_{bind} = G_{complex} - G_{receptor} - G_{ligand} \tag{1}$$

$$\Delta G_{bind} = E_{gas} + G_{sol} - TS \tag{2}$$

$$E_{gas} = E_{int} + E_{vdw} + E_{ele} \tag{3}$$

$$G_{sol} = G_{GB} + G_{SA} \tag{4}$$

$$G_{SA} = \gamma \, SASA \tag{5}$$

Gas-phase, internal, Coulomb, and van der Waals energy are represented by the symbols Egas, Eint, Eele, and Evdw. The FF14SB force field terms were used to evaluate the Egas directly. Gsol, or solution-free energy, was computed using the polar (GGB) and non-polar (G) energies. Using a 1.4 Å water probe radius, the non-polar solvation-free energy (GSA) was calculated from the Solvent Accessible Surface Area (SASA). Nonetheless, the polar solvation (GGB) contribution was evaluated using the GB equation. Temperature and total entropy of the solute are denoted by S and T. The binding free energy of each residue was calculated using Amber18's MM/GBSA-binding free energy approach.[44]

Cell Culture Assays, Determination of Proinflammatory Cytokine

Cytotoxicity Assays

These formulations were evaluated on human skin using HaCaT keratinocytes from the American Type Culture Collection (ATCC Manassas, VA, USA) (ATCC PCS-201–012).

The HaCaT cells were cultured in EMEM (Lonza, Walkersville, MD, USA) at a low concentration of Ca^{2+} (0.03 mM), supplemented with 10% FBS and 1% penicillin/streptomycin (Invitrogen Inc., Carlsbad, CA, USA), at 37°C in a humidified incubator, to perform a cell viability assay of the obtained CR solution and PVA/CH/GO-CR. MTT tests were used to investigate the effects of CR solution and PVA/CH/GO-CR on the viability of HaCaT cells.[4] 96-well plates were seeded with 5×10^4 cells/well of HaCaT cells. Cells were exposed to CR solution and PVA/CH/GO-CR (10, 20, 30, 40, 80, and 160 µg/mL) for a full day afterwards. Following the treatment, each well received 100 µL of fresh media and 10 µL of MTT reagent (5 mg/mL) from Sigma-Aldrich, St. Louis, MO, USA. The culture medium was then withdrawn. For four hours, the plate was incubated at 37°C. After removing the medium, each well received 50 µL of DMSO, and the wells were incubated for 30 minutes. Using a microplate reader (Tecan, Mannedorf, Switzerland), absorbance was measured at 570 nm.[45] The results of the MTT experiment were expressed as the percentage of cells that were less viable than untreated (control) cells using the Turner BioSystems ModulusTM microplate reader, which is manufactured in California.[46,47]

In vivo Investigation

Experimental Design

Albino adult male rats, 8–12 weeks old and weighing 180–200 g, were obtained from the Alexandria University animal sanctuary in Egypt. After acclimatization for a week under consistent light–dark cycles, controlled temperature (22–25 ° C), and humidity (45–60%), the rats were housed in cages with access to water and pellets. Ethical approval was obtained from the Alexandria University, and Faculty of Medicine Animal Ethics protocol was approved by the Institutional Animal Care and Use Committee (IACUC), Faculty of Medicine, Alexandria University (Approval ID: 0306488).

Induction of Diabetes and Excisional Skin Wound

A single intraperitoneal injection of 60 mg/kg streptozotocin (STZ) was used to induce diabetes. The blood from the rats' tail vein was drawn 72 h after STZ injection to determine the blood glucose level using a glucometer (ACCU Check, Roche, Basel, Switzerland). The rats were considered diabetic when the blood glucose level was higher than 250 mg/dL.[4] The blood glucose level was measured weekly to confirm the maintenance of hyperglycemia. Briefly, anaesthesia was induced using ketamine (80 mg/kg), and excision wounds (4 cm long, 2 mm deep) were created on the rats' dorsal area using an electric clipper after shaving. To reduce postoperative pain, buprenorphine was given intraperitoneally every 8 to 12 hours at a rate of 0.05 mg/kg.[1]

Experimental Grouping

A total of 45 rats were randomly assigned to five groups (n = 9): Group I (Diabetic untreated), another four diabetic groups were treated, Group II (diabetic group treated by Mebo and Gentamycin), Group III was treated with Cranberry (CR) powder, Group IV was treated with GO-CR, and Group V was treated with PVA/CH/GO-CR, the treatments were applied every day for 14 days.

Inflammatory Biomarker Measurement

After rats were given lipopolysaccharide (LPS) (10 mg/kg) for three hours, serum was taken from the tail vein.[48] According to the manufacturer's instructions, the concentrations of all cytokine ELISA kits (Excell Shanghai, China), the serum levels of inflammatory cytokines, such as pyrin domain-containing protein 3 (NLRP3) (Cat. No. KCD04232, Beijing AVIVA Systems Biology co., China), TNF-α (Cat. No abx050220, Abbexa, Ca, UK), IL-1β, and IL-6 (Cat. Nos. SEA563Ra and SEA079Ra, respectively, Cloud-clone Corp., TX, USA), were measured. The levels of these cytokines were calculated according to standard curves.[29]

Percentage of the Wound Closing

The intricate wound-healing process restores injured skin. This method relies on wound contraction to shrink the wound. At several treatment stages, the wound area is examined for closure. The steady decrease in wound size, usually expressed as a percentage, is called "wound contraction". Wound contraction % is calculated using this equation: Wound contraction percentage = 1-(Ax/A0) x 100.

A0 represents the wound area on day zero (the original measurement), and Ax represents the wound area at x day.[1]

Histopathological and Immunohistochemical (IHC) Examination of Vascular Endothelial Growth Factor (VEGF)

On days 3, 7, and 14, skin tissue samples from the wound sites were histologically analyzed to measure the degree of wound healing. In the pathology lab, the samples were properly preserved in 10% buffered formalin and stained with hematoxylin and eosin for histological examination.[4] The samples were prepared for immunohistochemical examination by the manufacturer's instructions using an IHC staining kit (InvitrogenTM, CA, USA). Using ABclonal's VEGF primary antibody at a 1:200 dilution, each group was incubated for an entire night by the primary antibody's instructions. Following incubation, sections were stained with 3.3′-diaminobenzidine tetrahydrochloride (Genemed Biotechnologies Inc., USA), and secondary antibodies and horseradish peroxidase were added. After applying Mayer's hematoxylin as a counterstain, the sections were assessed using ImageJ version K 1.45. To quantify parameters as a proportion of the entire region, we randomly picked five non-overlapping fields at 40× magnification for the study.[49]

Statistical Analysis

The in vitro data mean ± SD was shown. Conversely, the in vivo data displayed the median and interquartile change or mean ± SEM. Using SD and mean, group differences were investigated. In SPSS Statistics, a one-way ANOVA was carried out.[50] To determine statistical significance, Tukey's post hoc test used multiple comparison p-values of ≤0.05. Kruskal–Wallis and Dunn were utilized to analyze non-parametric score data. Data were statistically evaluated using Graph Pad Prism 8.0.2 (La Jolla, CA, USA).

Results and Discussion

HPLC Analysis for Identification of Components Present in the Cranberry Powder

The phenolic and flavonoid components of CR powder were isolated and quantified using HPLC. Table 1 and Figure 1 S show seventeen peaks being detected at 250 nm. Compounds like Vanillin, Ferulic acid, Rosmarinic acid, Quercetin, Cinnamic acid, and Kaferol were measured as significant phenolic acids for these peaks. Other phenolic acids were gall, Chlorogenic, Methyl gall, Caffeic, Syringic, Ellagic, and Coumaric acids. Peak flavonoids include naringenin, daidzein, quercetin, kaempferol, and hesperetin, which have been identified according to their retention times, and the spectral

Table 1 Compound, Retention Times, and Area Peaks of Cranberry Powder

Peak no.	Compounds	Retention Time	Area %	Conc (µg/mL)
1	Gallic acid	3.59	46.44	549.16
2	Chlorogenic acid	4.15	0.46	8.33
3	Catechin	4.39	3.39	103.38
4	Methyl gallate	5.08	0.98	6.75
5	Caffeic acid	5.83	0.37	4.08
6	Syringic acid	6.43	28.90	289.79
7	Ellagic acid	7.28	1.87	29.71
8	Coumaric acid	8.70	4.36	22.01
9	Vanillin	9.26	2.20	21.56
10	Ferulic acid	9.99	4.77	11.13
11	Naringenin	10.51	1.02	38.66
12	Rosmarinic acid	12.26	0.23	3.37
13	Daidzein	16.33	0.72	5.58
14	Quercetin	17.38	1.31	22.20
15	Cinnamic acid	19.04	1.91	4.72
16	Kaempferol	20.78	0.48	4.23
17	Hesperetin	21.07	0.58	3.98

characteristics of their peaks against those of standard powdered cranberry, gallic acid, and syringic acid were found to be the most abundant phenolic components at 549.16 µg/mL and 289.79 µg/mL, respectively. Quercetin was found to be the most abundant flavonoid component at 22.20 µg/mL. These components are known for their potential therapeutic properties, including antioxidant and anti-inflammatory effects, which can be beneficial in promoting wound healing.[9]

In vitro Characterization of Electrochemical Exfoliation of GO and Hydrogel

Graphene oxide (GO) has recently gained attention for tissue regeneration in skin and bone applications due to its unique properties, including conductivity, antimicrobial activity, and mechanical strength.[51,52] Traditionally, GO is synthesized using chemical exfoliation, a process that involves harsh oxidants and poses risks of explosion, environmental contamination, and extended reaction times.[53] In contrast, electrochemical exfoliation (movie1) offers a safer and more efficient approach for producing GO. This method uses a graphite electrode subjected to an electric potential in an electrolyte solution, such as zinc nitrate or sodium chloride, causing the graphite layers to expand and separate into GO sheets. This technique provides fine control over the thickness and functional group density of GO, making it particularly suited for biomedical applications. Additionally, electrolytes like zinc nitrate influence the structural and defect properties of the synthesized GO. Notably, in this study, the GO produced had a dark yellow colour, which changed to dark brown upon the addition of cranberry extract (Figure 1a and b). Cranberry extract was selected for its well-documented antioxidant, anti-inflammatory, and anti-biofilm properties. The phenolic compounds and flavonoids in the extract likely interact with the oxygen-containing functional groups of GO (such as hydroxyl, carboxyl, and epoxy), contributing to the formation of nanoparticle-like clusters on the GO nanosheets, as observed in TEM images (Figure 1c). These Zn-cranberry clusters may attach to the GO surface through electrostatic interactions and π-π stacking. Similar nanostructures were reported in previous studies where curcumin loaded onto GO formed nanoclusters[54], and GO functionalized with Tamarindus indica extract and zinc ions also exhibited nanoparticle aggregates.[55] The primary objective of this work was to develop a multifunctional hydrogel to accelerate diabetic wound healing. GO-CR (GO with cranberry) was blended with PVA/CH (polyvinyl alcohol/chitosan), and boric acid was added as a crosslinker. In contrast to uncross-linked PVA/CH films (Figure 1d), which showed an irregular surface, SEM analysis of the hydrogel revealed a fiber-like structure (Figure 1e). This morphology is likely due to the large surface area of GO, which serves as a template for the alignment of PVA chains and cranberry-derived compounds, promoting the formation of fibrous structures within the hydrogel matrix. The self-healing properties of the hydrogel are particularly advantageous for wound healing applications. The material's ability to repair itself after damage ensures the dressing's structural integrity and extended functionality, reducing the

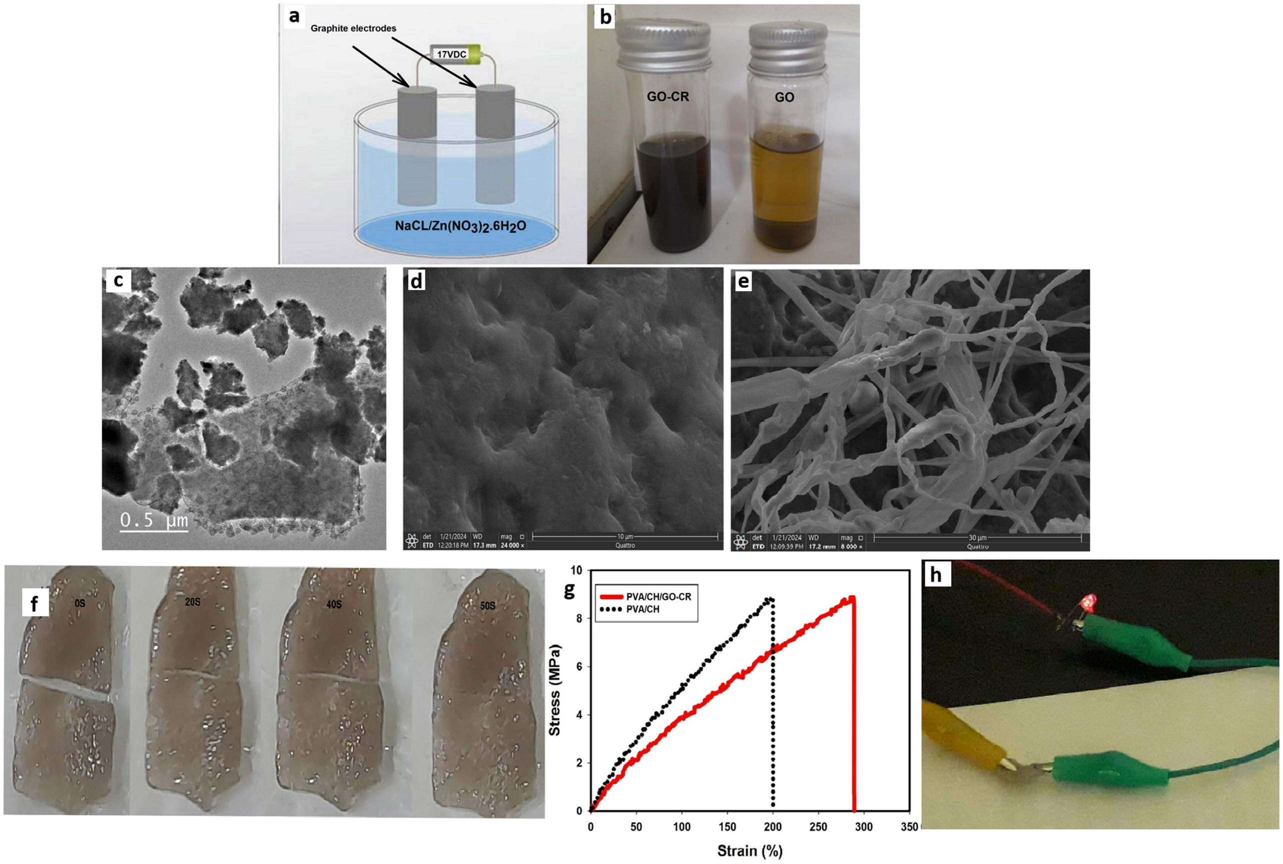

Figure 1 (**a**) Electrochemical cell for GO fabrication (**b**) GO and GO-CR produced, (**c**)TEM image of GO-CR (**d**) SEM image of PVA/CH cast film (**e**) SEM image of PVA/CH/GO-CR, (**f**) Self-healing property of PVA/CH/GO-CR hydrogel (**g**) Mechanical property of PVA/CH and PVA/CH/GO-CR and (**h**) Electrical conductivity of PVA/CH/GO-CR.

need for frequent replacement and minimizing infection risk. Additionally, the self-healing ability allows the hydrogel to adapt to the dynamic conditions of the wound site, such as movement and stretching, improving tissue integration and promoting faster healing. In our study, the PVA/CH/GO-CR hydrogel self-healed in approximately 50 seconds (Figure 1f). Previous work demonstrated that hydrogels cross-linked with borax, including silver nanoparticles, also exhibited rapid self-healing, likely due to the combined effects of zinc content and phenolic hydroxyl groups in cranberry extracts. The stretching capacity of PVA/CH/GO-CR was 280%, significantly higher than that of PVA/CH (200%), attributed to the enhanced electrostatic and hydrogen bonding interactions (Figure 1g). A similar effect was observed in hydrogels incorporating ZnO nanoparticles, which improved electrostatic crosslinking and mechanical properties.[11,56]

Endogenous bioelectrical signalling plays a key role in tissue regeneration, especially in electro-sensitive tissues like skin.[57,58] By promoting cell-to-cell communication, conductive materials such as GO-based hydrogels accelerate cell migration and wound closure (46). In this study, PVA/CH/GO-CR demonstrated excellent electrical conductivity, attributable to the GO content and the presence of sodium and zinc ions (Figure 1h).[58,59] The FTIR spectrum of PVA/CH revealed a broad band between 3200 and 3700 cm^{-1} corresponding to OH and NH stretching and a peak at 1643 cm^{-1} for C=O stretching.[60] These peaks intensified significantly in PVA/CH/GO-CR, reflecting the abundant hydroxyl and carbonyl groups from both cranberry extract and GO (Figure 2a). In this study, the hydrogel exhibited a photothermal-driven exudate removal mechanism, where the GO content significantly enhanced photothermal conversion.[61] Upon exposure to light, the temperature of PVA/CH/GO-CR increased to approximately 44 °C, compared to 31 °C for PVA/CH (Figure 2b), facilitating water loss and exudate evaporation. The hydrogel lost 36% of its total weight within 9 minutes of light exposure (Figure 2c), a significant improvement over conventional PVA/CH hydrogel. Similar photothermal-induced exudate evaporation has been previously demonstrated using charcoal nanoparticles

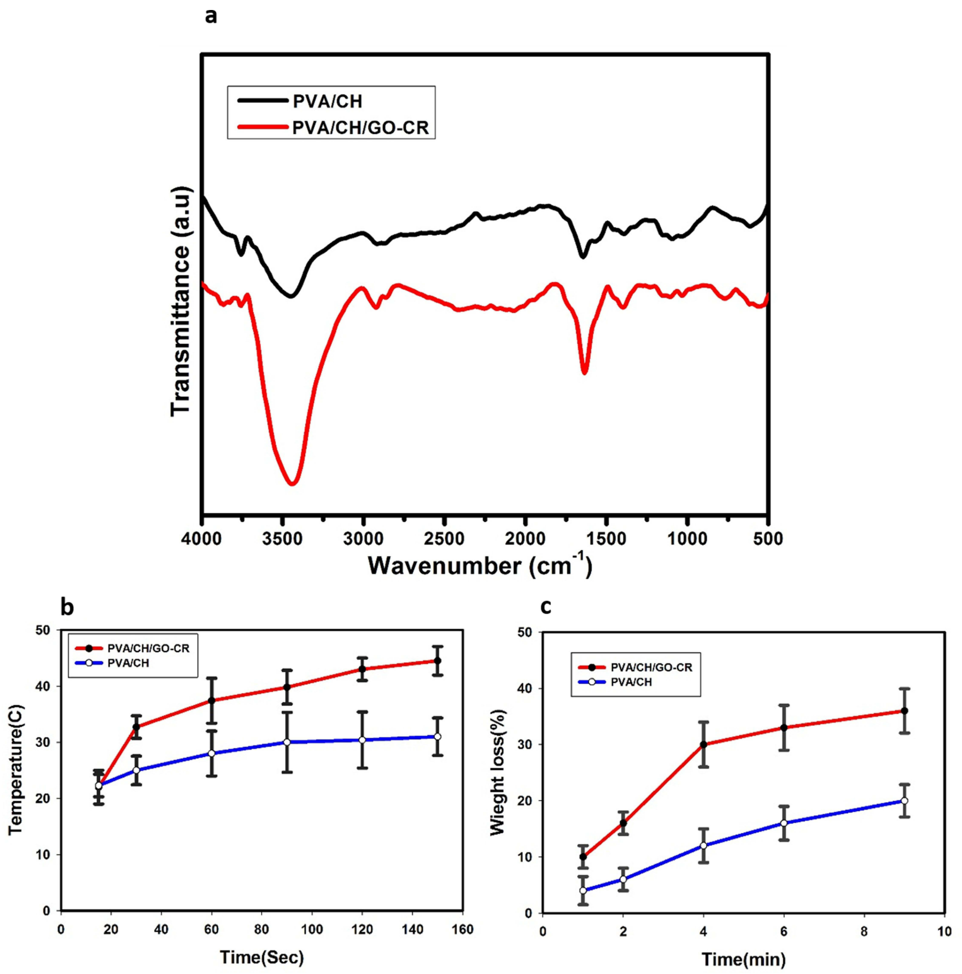

Figure 2 (**a**) FTIR spectrum of PVA/CH and PVA/CH/GO-CR hydrogel, (**b**) The photothermal effect on both PVA/CH and PVA/CH/GO-CR and (**c**) the photothermal induced water loss of both PVA/CH and PVA/CH/GO-CR.

embedded in polyurethane nanofibers.[62,63] It was demonstrated that the temperature of PVA/CH/GO-CR reached approximately 44 °C after exposure to the light for 150 Sec, compared to 31 °C for PVA/CH (Figure 2b). In conclusion, this multifunctional PVA/CH/GO-CR hydrogel, with its self-healing, conductive, and photothermal properties, presents a promising solution for enhancing diabetic wound healing.[52]

Assay for Antioxidant Activity

Oxidative stress, implicated in degenerative diseases, occurs when the body's natural defences against free radicals, known as antioxidants, are overwhelmed, leading to the oxidation of proteins and fats. Antioxidants derived from medicinal plants are vital to overall health.[49] In this study, the stable free radical DPPH, which exhibits a yellow colour change in the presence of antioxidants, was employed to assess the antioxidant activity of CR, PVA/CH/GO-CR. By contributing hydrogen radicals (H•), antioxidants scavenge the DPPH radical, forming stable DPPH-H molecules. As depicted in Figure 3, the ability of ascorbic acid and nanoparticles to scavenge radicals increased with rising concentrations. Table 2 presents the concentration required to scavenge 50% of the DPPH radical, denoted by the IC_{50} values, which are 7.12 ± 0.33 µg/mL for CR, 6.43 ± 0.42 µg/mL for PVA/CH/GO-CR, and 10.43 ± 0.21 µg/mL for ascorbic acid.[64] These findings align with previous research and demonstrate the robust antioxidant capability of the nanoparticles, surpassing the benchmark set by ascorbic acid. Incorporating multiple phytochemicals, likely working synergistically to combat free radicals, contributes to the antioxidant activity of the nanoparticles. These results offer compelling evidence

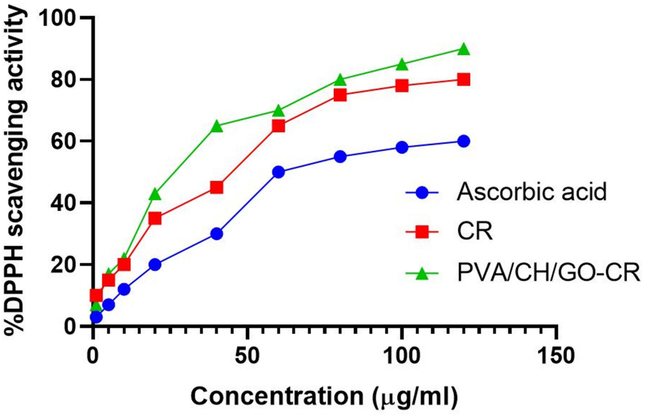

Figure 3 Effect of CR and PVA/CH/GO-CR on HSE-2 cell viability. Cell viability of 100% corresponds with untreated cell MTT average reduction value. n = 6, P-value <0.006.

for utilizing naturally occurring antioxidants, such as PVA/CH/GO mediated by cranberry and derived from floral extracts, as a strategy for mitigating oxidative stress associated with degenerative diseases.[1,45]

Antimicrobial Assay

Antibacterial Effect

CR, GO-CR, and PVA/CH/GO-CR hydrogels demonstrated antibacterial activity against *S. epidermidis, Pseudomonas aeruginosa K. pneumoniae*, and *E. coli*, The results indicated that they exhibited a broad spectrum of antibacterial effects against both gram-positive and gram-negative isolates. The most significant antibacterial effect was observed with the PVA/CH/GO-CR hydrogel. Inhibition zones *against S. epidermidis, Pseudomonas*, and *E. coli* were recorded at 34.5 ± 0.32 mm, 32.5 ± 0.12 mm, and 24.5± 0.43 mm, respectively; meanwhile, with GO-CR, inhibition zones were measured at 32.5 ± 0.21 mm and 32.16 ± 0.32 mm 23.5 ± 0.34 mm, respectively. Furthermore, cranberry powder exhibited in inhibition zones recorded 30.5 ± 0.51 mm and 29.5 ± 0.50 mm, 20.5± 0.32 mm, respectively. While the inhibition zones were slightly smaller, measuring with *K. pneumoniae*, cranberry powder(C), Green graphene cranberry (G), and their PVA/CH/GO-CR hydrogel (N) were all as depicted in Figure 4 and Table 3.

Antibiofilm Activity

Cranberry extract, GO cranberry nanosheet, and PVA/CH/GO-CR hydrogel showed antibiofilm properties against gram-positive and negative isolates. The results indicate that Cranberry powder (C), Green graphene oxide nano-sheet (G), and PVA/CH/GO-CR hydrogel (N) inhibited biofilm formation. After 24 hours, the reduction percentages for *S. epidermidis* biofilm as an example of a gram-positive strain were 62%, 59%, and 49%, while in the case of *Pseudomonas*, reduction percentages were 75%, 59%, and 56% as a gram-negative isolate, and in *E. coli*, it was 41%, 38%, and 37%, respectively, while *K. pneumoniae* was the least one of gram-negative organism which shows 9%,10% and 16%, respectively, as shown in Figure 5a and b.

Figure 5b. The first lane showed positive biofilm formation, and subsequent lanes from left to right showed the effect of Green cranberry graphene oxide nanosheet (N), Graphene oxidase nanosheet (G), and Cranberry powder (C) caused a reduction of biofilm formed by *S. epidermidis* (I), *Pseudomonas* (2), *E. coli* (3) and *K. pneumoniae* (4) after 24 hours, respectively. The World Health Organization emphasizes how urgently new antibiofilm agents and compounds are

Table 2 The IC_{50} of PVA/CH/GO-CR and Ascorbic Acid in the DPPH Test

	CR	PVA/CH/GO-CR	Ascorbic acid
IC_{50} of DPPH	7.12 ± 0.33 µg	10.43 ± 0.21 µg	6.43 ± 0.42 µg

Note: IC50 is the concentration of CR that can scavenge DPPH radicals by 50%.

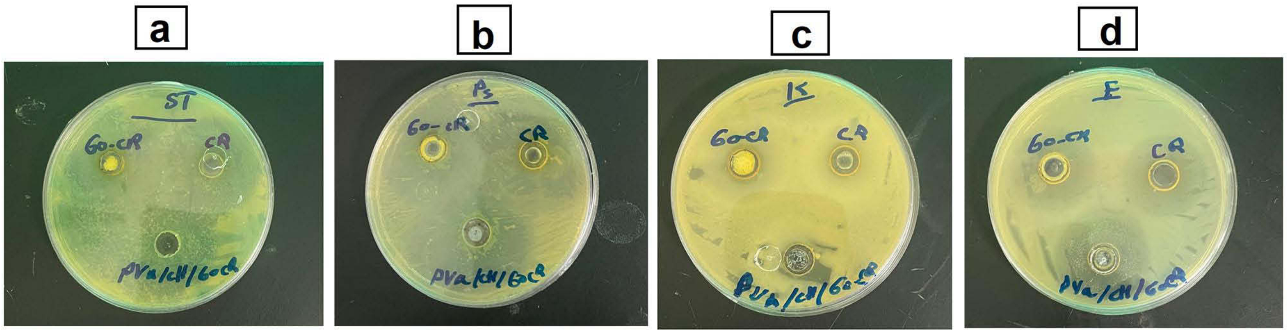

Figure 4 Antibacterial effect of CR, GO-CR, and PVA/CH/GO-CR against *S. epidermidis* (**a**), *Pseudomonas aeruginosa* (**b**) *K. pneumoniae* (**c**), and *E. coli* (**d**).

needed to combat antibiotic resistance, which is predicted to cause a significant amount of death. Because of this toxic tolerance, treatment is a therapeutic method for slow-growing microorganisms. However, by overcoming physiological barriers and using nanoparticles as carriers, nanotechnology, especially nanomedicine, has revolutionized disease diagnosis and therapy. Additionally, the matrix containing microorganisms is permeabilized by nanoparticles, allowing them to penetrate the pore diameter of biofilms and improving their accessibility.[65] It has been shown that a class of compounds originating from plants called polyphenols can alter the human microbiota, either by promoting the growth of good microbes or suppressing the growth of harmful ones. Furthermore, cranberries contain phenolic acids, proanthocyanidins, anthocyanins, organic acids, and microbial metabolites that specifically inhibit intestinal infections, reduce bacterial adhesion and motility, and limit *Pseudomonas* pathogenicity. The current findings corroborate earlier research in both in vitro and in vivo contexts, showing that cranberry extracts, fractions, and components are efficient against a variety of harmful microorganisms,[9] including those causing urinary tract infections (UTIs) and other illnesses and researched graphene oxide nanosheets as a synthetic nanomaterial with a hydrophobic plane structure that efficiently suppresses both gram-positive and gram-negative bacteria. Amphipathic GO nanosheets can kill bacteria without the need for intracellular processes. Moreover, cranberry powder inhibits the growth of *E. coli* biofilms by reducing biofilm formation. Reducing adhesion might lessen the development of biofilms. Using complicated nanoparticles (NPs) up to 1000 nm in size, which are distinguished by their tiny size and complex interactions with their surroundings, nanotechnology improves drug development.

Additionally, the functionality and structure of the biofilm surface are altered by nanomaterials, allowing nutrients and negatively charged and hydrophobic groups to pass through water-filled pores. Nanomaterial biofilm penetration is influenced by size and electrostatic interactions. While cationic nanoparticles diffuse throughout the matrix, uncharged nanoparticles move effectively via biofilm pores smaller than 350 nm.[31]

Our research shows that graphene oxide nanosheets exhibit an antibacterial effect and antibiofilm activity against gram-negative and positive bacteria, with activity after 24 hours of biofilm development. We discovered that graphene oxide effectively reduces biofilms of *S. epidermidis, Pseudomonas, E. coli*, and K. *pneumoniae* after 24 hours due to its

Table 3 The Effect of Cranberry Powder (C), Green Graphene Cranberry (G), and Their PVA/CH/GO-CR Hydrogel (N) on Zone Inhibition, MIC and MBC with the Most Effective 3 Isolates Pseudomonas, S. Epidermidis, and E. Coli Respectively

Strain	**Zone Inhibition (mm)**			**MIC (mg/ mL)**			**MBC (mg/ mL) at 0 time**		
	C	**G**	**N**	**C**	**G**	**N**	**C**	**G**	**N**
Pseudomonas	29.5±0.50	32.16±0.32	32.5±0.12	10±0.12	10±0.04	10±0,02	25±0.04	30±0,04	30±0.31
S.epidermidis	30.5±0.51	32.5±0.21	34.5±0.32	25±0.01	24±0.11	22±0.05	50±0.05	50±0.31	50±0.42
E. coli	20.5±0.32	23.5±0.34	24.5±0.43	8±0.25	8±0.03	10±0.03	18±0.12	20±0.0.21	20±0.31

Abbreviations: MIC, the minimum inhibitory concentration; MBC, the minimum bactericidal concentration.

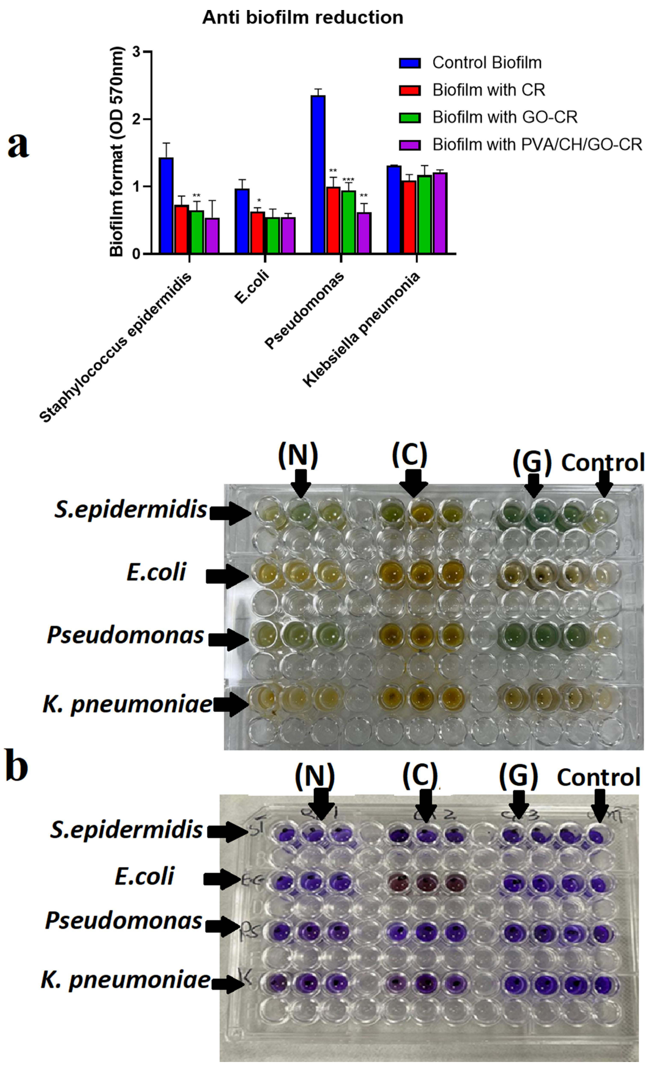

Figure 5 (a). Antibiofilm reduction effect of *S. epidermidis* (1), *Pseudomonas* (2) *K. pneumoniae* (3), and *E. coli* (4).**(b)**. Crystals violet assay to assess antibiofilm activity of Green cranberry graphene oxide nanosheet (**N**), Cranberry extract (**C**), and Graphene oxidase nanosheet (**G**).
Note: P value ***= 0.0001, **= 0.0079, and *=0.0444.

hydrophilic carbon-rich surface interaction. Thus, the Green cranberry graphene oxide nanosheet effectively reduces microbial growth and adhesion to surfaces and each other, maintaining its antibiofilm effect over various periods.

In silico Study

Molecular Dynamic and System Stability

A molecular dynamic simulation predicted the performance of extracted chemicals binding to the protein's active site, interaction, and stability. System stability must be validated to track interrupted motions and avoid simulation artifacts.[2,36] This study measured system stability using Root-Mean-Square Deviation (RMSD) in 20 ns simulations. The average RMSD values for system frames were 1.87 ± 0.40 Å and 1.74 ± 0.33Å for VEGF-Apo complex and VEGF-Rosmarinic acid-complex, respectively (Figure 6a. I), 3.65 ± 0.61Å and 3.61 ± 0.9Å for NanE-Apo complex and TNF-alpha-Apo complex, respectively (Figure 6b. I), and 1.29 ± 0.25 and 1.13 ± 0.17Å for TNF-alpha-Apo complex, respectively (Figure 6c. I). These findings showed that the Rosmarinic acid-bound to protein complex system was more stable than the others. For residue behavior and ligand interaction in MD simulation, protein structural flexibility must be assessed upon ligand binding.[66] Over 20 ns simulations, the Root-Mean-Square Fluctuation (RMSF) technique was used to assess inhibitor binding to target protein residues. Average RMSF values were 7.78 ± 0.12 Å and 5.92 ± 0.37Å for VEGF-Apo complex and VEGF-Rosmarinic acid-complex, respectively (Figure 6a. II), 1.67 ± 0.52Å and 1.30 ± 0.08Å for NanE-Apo complex and NanE-Rosmarinic acid complex (Figure 6b. II), 1.15 ± 0.61 Å and 1.00 ± 0.49Å for TNF-alpha-Apo complex and TNF-alpha-Rosmarinic acid-complex, respectively (Figure 6c. II). This showed that the Rosmarinic acid-bound to protein complex system had more residue variability than the others. ROG assessed the system compactness and stability by MD simulation with ligand binding.[4] Rg values averaged 23.79 ± 0.19Å and 23.46 ± 0.17Å for VEGF-Apo complex and VEGF-Rosmarinic acid-complex, respectively (Figure 6a. III), 17.55 ± 0.16Å and 17.27 ± 0.10Å for NanE-Apo complex and NanE-Rosmarinic acid complex, respectively (Figure 6b. III), and 15.77 ± 0.12 and 15.63 ± 0.07Å for TNF-alpha-Apo complex and TNF-alpha-Apo

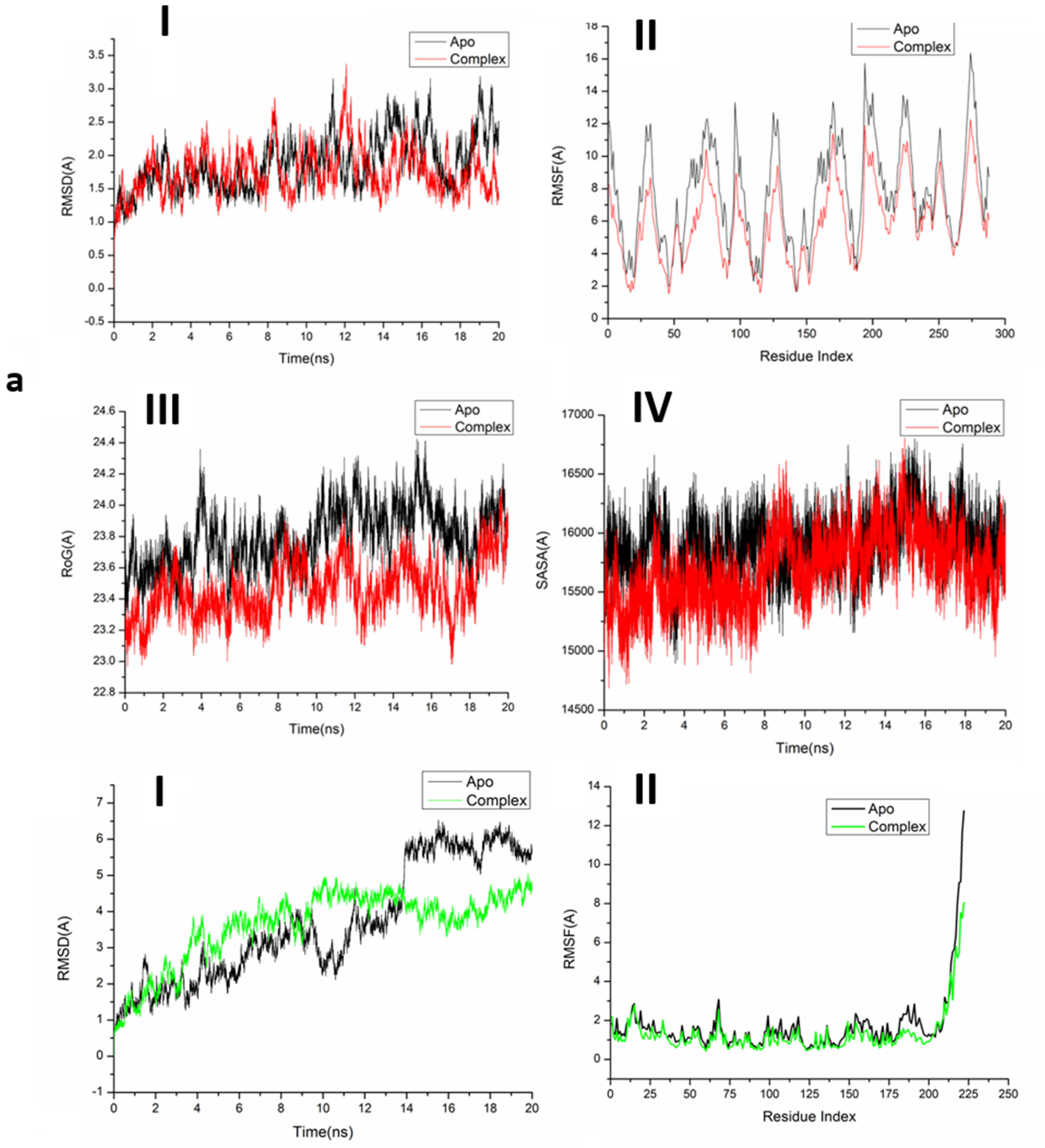

Figure 6 Continued.

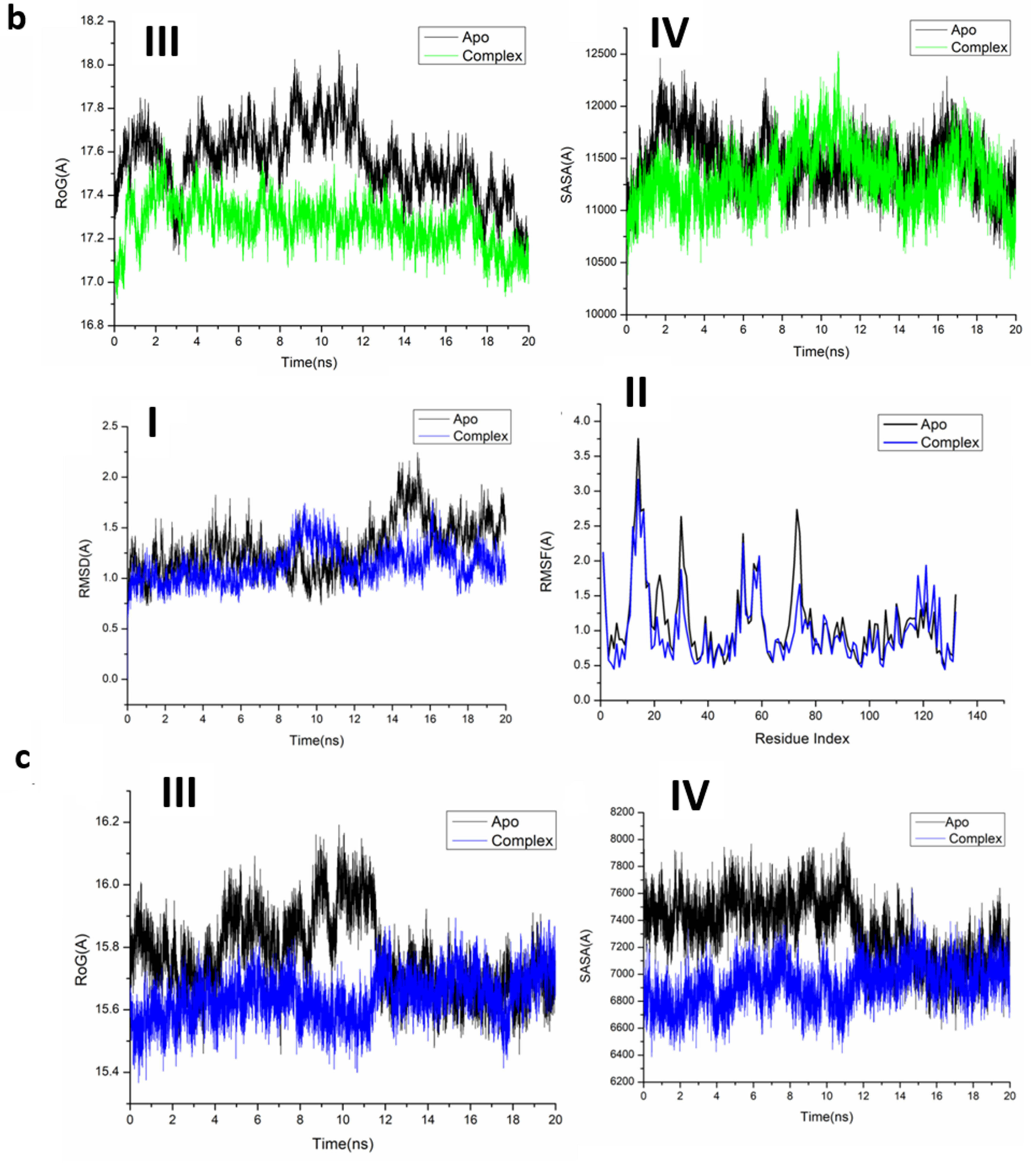

Figure 6 RMSD of Cα atoms of protein backbone atoms(**a**–**c**) (I). (II) RMSF of each residue of the protein backbone Cα atoms of protein residues; (III) ROG of Cα atoms of protein residues; (**a**) (IV) solvent accessible surface area (SASA) of the Cα of the backbone atoms relative (black) to the starting minimized over 20 ns for the ATP binding site of the VEGF receptor with Rosmarinic acid (red); (**b**) (IV) solvent accessible surface area (SASA) of the C α of the backbone atoms relative (black) to the starting minimized over 20 ns for the ATP binding site of the NanE receptor with Rosmarinic acid (green); and (**c**) (IV) solvent accessible surface area (SASA) of the C α of the backbone atoms relative (black) to the starting minimized over 20 ns for the TNF-alpha receptor with Rosmarinic acid (blue).

complex, respectively (Figure 6c. III). Based on its behavior, Rosmarinic acid has a highly stiff structure against VEGF, NanE, and TNF-alpha receptors. The protein's solvent-accessible surface area was calculated to determine its hydrophobic core compactness. Measuring the protein's solvent-visible surface area is critical for biomolecule stability.[49] The average SASA values for VEGF-Apo complex and VEGF-Rosmarinic acid-complex were 15905.75Å and 15699.23Å, respectively (Figure 6a. IV), 11,452.75Å and 11312.89Å for NanE-Apo complex and NanE-Rosmarinic acid complex, respectively (Figure 6b. IV), and 7341.76Å and 6919.30Å for TNF-alpha-Apo complex and TNF-alpha-Rosmarinic acid-complex, respectively (Figure 6c. IV). The SASA discovery, along with the RMSD, RMSF, and ROG computations, confirmed that the Rosmarinic acid complex system remains intact in the catalytic domain-binding site of VEGF, NanE, and TNF-alpha receptors.

Binding Interaction Mechanism Based on Binding Free Energy Calculation

The free-binding energies of small molecules to biological macromolecules are commonly measured using the molecular mechanics energy methodology (MM/GBSA), which combines the generalized Born and surface area continuum solvation. This method may be more accurate than docking scores by taking snapshots from the systems' trajectories. The binding free energies were calculated using AMBER18's MM-GBSA program.

Table 4 shows that all reported computed energy components had significant negative values indicating beneficial interactions, except ΔGsolv. A detailed analysis of each energy contribution, which provides the stated binding free energies, indicates that the interactions between the rosmarinic acid molecule and the VEGF and NanE receptor protein residues are driven by the higher positive electrostatic energy components. On the other hand, the interactions between the TNF-alpha receptor protein residues and the rosmarinic acid molecule are facilitated by the increased positive Vander Waals energy components.

Identification of the Critical Residues Responsible for Ligand Binding

To learn more about key residues involved in the inhibition of the VEGF, NanE and TNF-alpha receptor by Rosmarinic acid compound, the total energy involved when Rosmarinic acid compound contacts these enzymes were further broken down into the involvement of site residues from Figure 7a, the major favourable contribution of Rosmarinic acid compound to the VEGF receptor is predominantly observed from residues Asp 22(−3.9 kcal/mol), Ile23 (−0.86 kcal/mol), Phe24 (−0.446 kcal/mol), Ile34 (−2.689 kcal/mol), Phe35 (−1.063 kcal/mol), Ser 38(−0.924 kcal/mol), Cys39 (−0.92 kcal/mol), Ile 71 (−0.251 kcal/mol), Pro73 (−0.231 kcal/mol), Asn146 (−0.688kcal/mol), Asp 147 (−3.283 kcal/mol), Glu148 (−0.881 kcal/mol), Gly 149(−0.177 kcal/mol), Thr 284 (−0.111 kcal/mol), Hie285 (−0.985 kcal/mol), Arg 286 (−1.039 kcal/mol), Gln 287 (−0.466 kcal/mol), and Thr 288 (−0.629 kcal/mol). From Figure 7b, the major favourable contribution of the Rosmarinic acid compound to the NanE receptor is predominantly observed from residues Ile 7

Table 4 Shows the Calculated Energy Binding for the Rosmarinic Acid Compound Against the Catalytic Binding Site of VEGF, NanE, and TNF-Alpha Receptors

Energy Components (kcal/mol)					
VEGF					
Complex	**ΔE_{vdW}**	**ΔE_{elec}**	**ΔG_{gas}**	**ΔG_{solv}**	**ΔG_{bind}**
Rosmarinic acid	−29.58± 0.25	−72.88± 0.67	−102.46± 0.75	60.18± 0.43	−42.28± 0.39
NanE					
Rosmarinic acid	−27.61± 0.23	−79.35± 1.02	−106.97± 0.93	58.87± 0.57	−48.10± 0.41
TNF-alpha					
Rosmarinic acid	−22.18± 0.13	−5.35± 0.34	−27.50± 0.36	11.19± 0.24	−16.35± 0.16

Abbreviations: ΔEvdW, van der Waals energy; ΔEele, electrostatic energy; ΔGsolv, solvation free energy; ΔGbind, calculated total binding free energy.

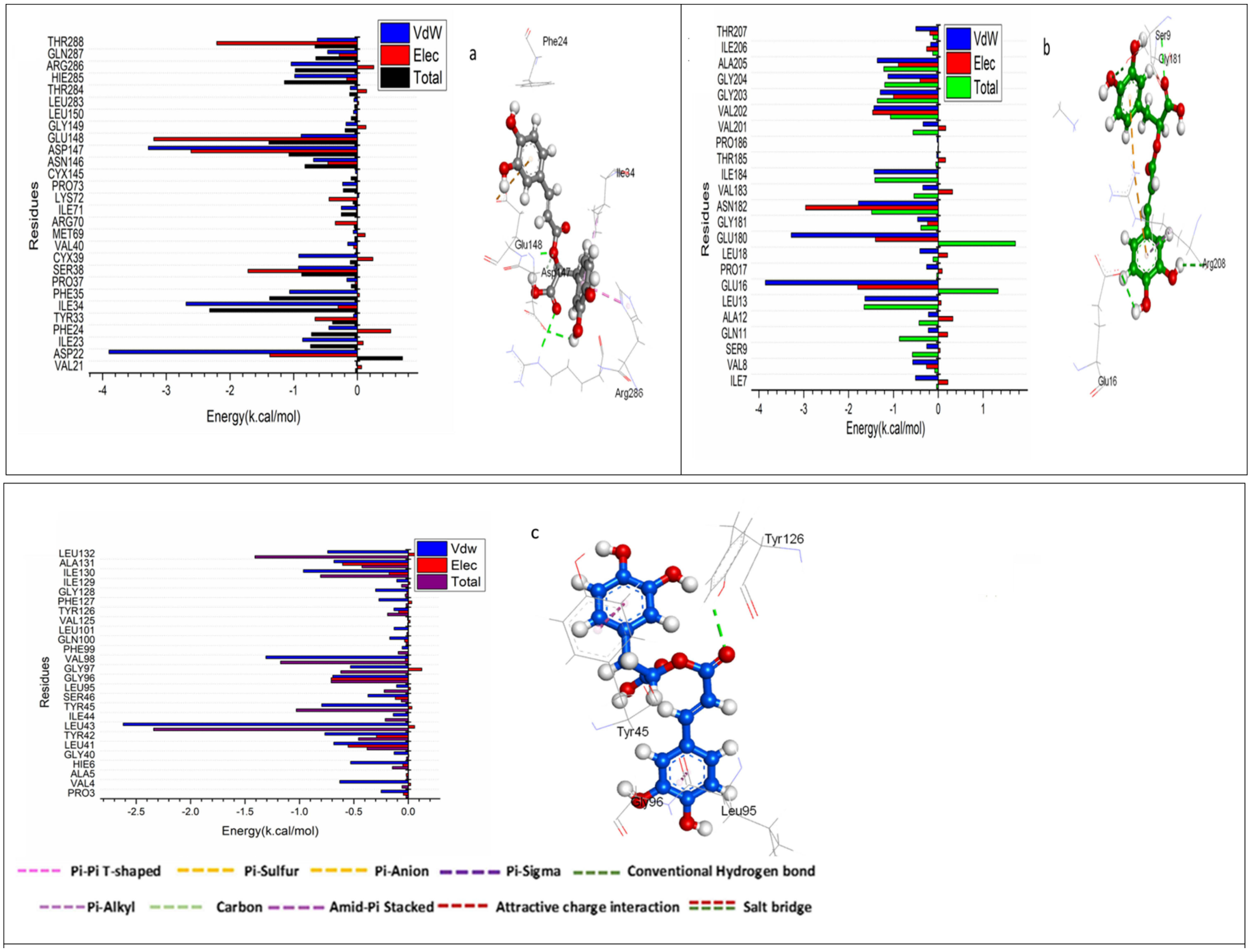

Figure 7 Per-residue decomposition plots show the energy contributions to the binding and stabilization of 9- Rosmarinic acid to the ATP binding site of VEGF (**a**), NanE (**b**), and TNF-alpha (**c**).

(−0.51 kcal/mol), Val 8 (−0.57 kcal/mol), Ser9 (−0.258 kcal/mol), Gln11 (−0.224 kcal/mol), Ala 12 (−0.22 kcal/mol), Leu 13 (−1.636 kcal/mol), Glu 16 (−3.857 kcal/mol), Pro 17(−0.26 kcal/mol), Leu 18 (−0.41 kcal/mol), Glu 180 (−3.281 kcal/mol), Gly 181 (−0.46 kcal/mol), Asn 182 (−1.78 kcal/mol), Val 183 (−0.344 kcal/mol), Ile 184 (−1.433 kcal/mol), Val 201 (−0.339 kcal/mol), Val 202 (−1.435 kcal/mol), Gly 203 (−1.295 kcal/mol), Gly 204 (−1.124 kcal/mol), Ala205 (−1.361 kcal/mol), and Ile 206 (−0.17 kcal/mol).

Finally, from Figure 7c the major favourable contribution of Rosmarinic acid compound to the TNF-alpha receptor is predominantly observed from residues Pro 3 (−0.25 kcal/mol), Val 4 (−0.63 kcal/mol), Hie 6 (−0.53 kcal/mol), Leu 41 (−0.684 kcal/mol), Tyr 42 (−0.766 kcal/mol), Leu 43 (−2.619 kcal/mol), Ile 44 (−0.138 kcal/mol), Tyr 45 (−0.796 kcal/mol), Ser 46 (−0.37 kcal/mol), Gly 96 (−0.694 kcal/mol), Gly 97 (−0.531 kcal/mol), Val 98 (−1.309 kcal/mol), Gln 100 (−0.17 kcal/mol), Phe 127 (−0.27 kcal/mol), Gly 128 (−0.3 kcal/mol), Ile 129 (−0.106 kcal/mol), Ile130 (−0.963 kcal/mol), Ala 131 (−0.683 kcal/mol), and Leu 132 (−0.741 kcal/mol).

Ligand–Residue Interaction Network Profiles

Docked VEGF Complexes

The docked Rosmarinic acid-VEGF complex showed that the carbonyl group of Rosmarinic acid has formed a hydrogen bond interaction with Tyr 126. It is worth noting that the pyrocatechol ring has formed A pi-pi interaction between Tyr 45 and Leu 95 (Figure 8a).

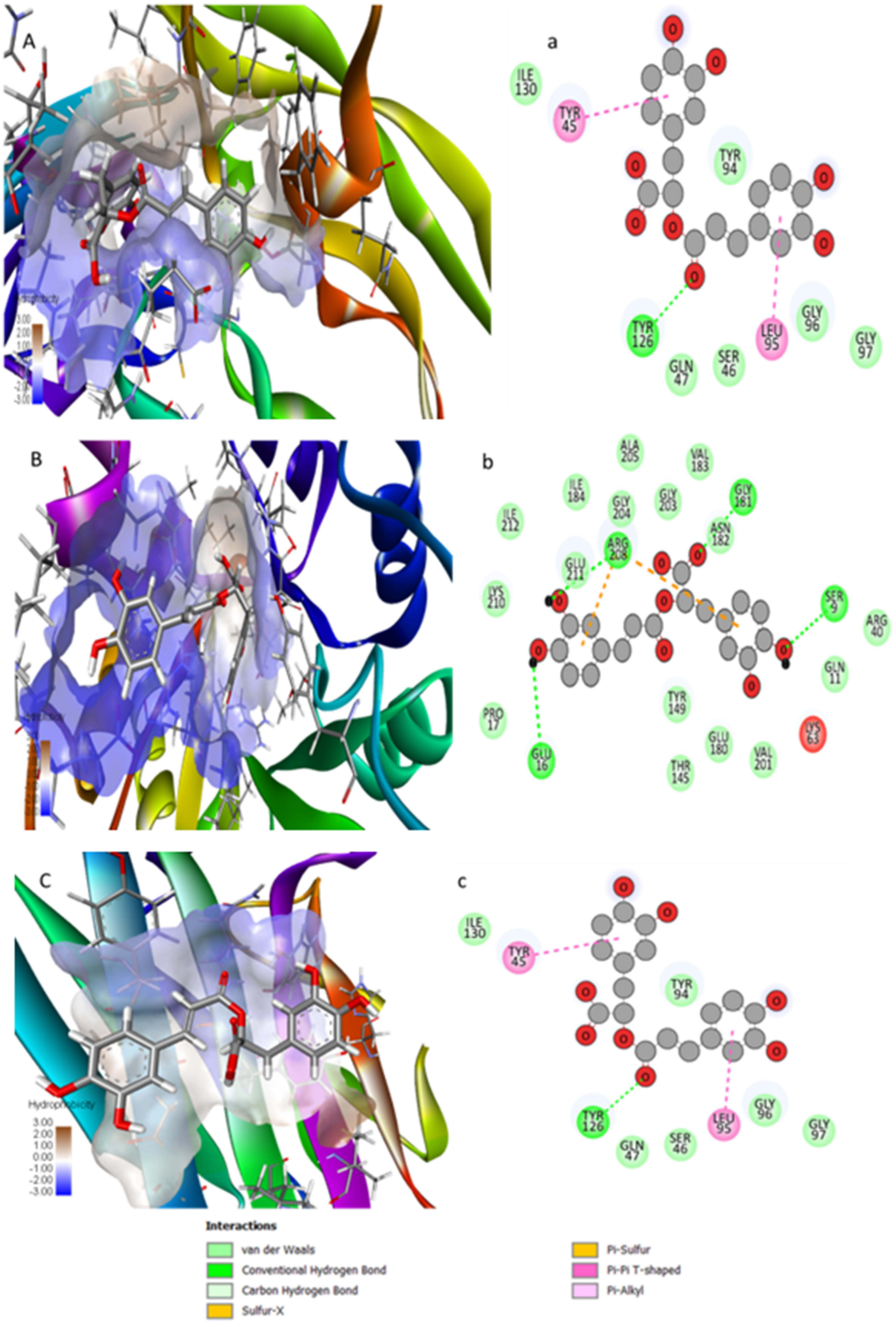

Figure 8 The Rosmarinic acid contact residue in the VEGF binding site (**a**), NanE binding site (**b**) and TNF-alpha binding site (**c**).

Docked NanE Complex

In Figure 8b, the docked NanE - Rosmarinic acid complex showed that the hydroxyl group of the pyrocatechol ring has formed a hydrogen bonding interaction with Ser 9 and Glu 16. Notably, the carboxylic acid group has established hydrogen bonding interaction with Gly 181. The pharmacophoric hot spot residue, Arg 208, has formed Hydrogen bonding, and Pia cation interactions with the pyrocatechol ring.

Docked TNF-Alpha Complex

In Figure 8C, the docked TNF-alpha - Rosmarinic acid complex showed that the carbonyl group of Rosmarinic acid has formed a hydrogen bonding interaction with Tyr 126. Notably, the pyrocatechol ring has formed Pi-Pi interaction with both Tyr 45 and Leu 95.

Cell Culture Assays, Determination of Proinflammatory Cytokine

Cytotoxicity Assays

As seen in Figure 9a, human skin keratinocytes (HaCaT) cells were used to evaluate the safety of the CR and PVA/CH/GO-CR hydrogel. Following a 24-hour incubation period, PVA/CH/GO-CR hydrogel concentrations as high as 80 µg/mL did not exhibit any harmful effects. Over 99% of the cells were still viable at all tested dosages. These findings suggest

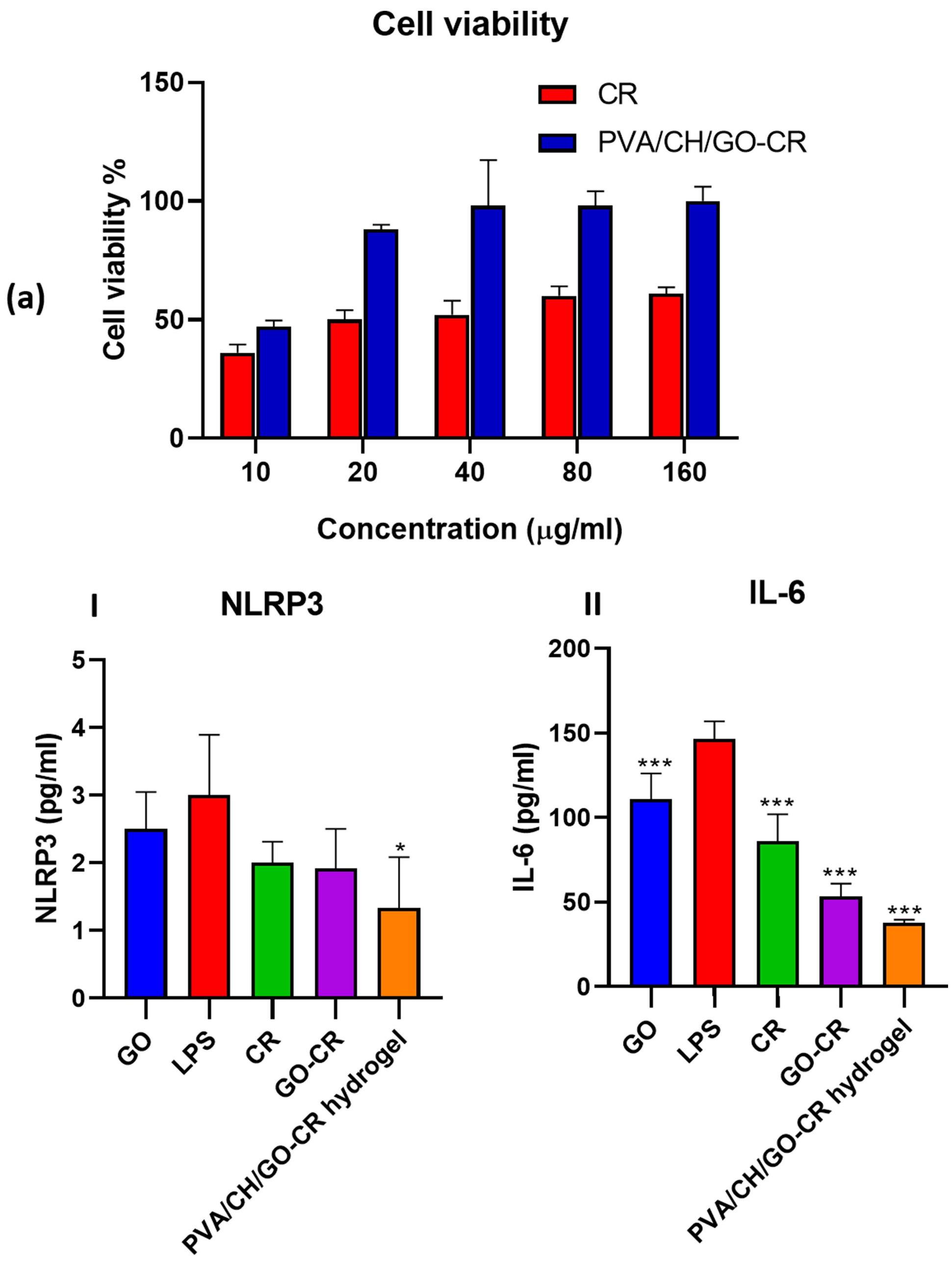

Figure 9 Continued.

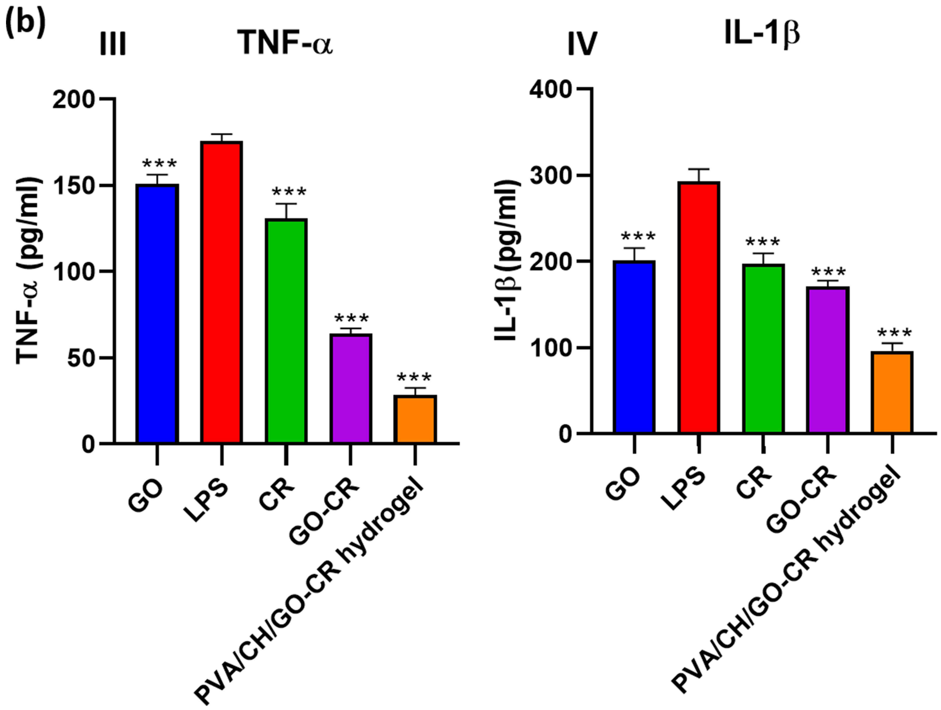

Figure 9 (**a**) Effect of CR and PVA/CH/GO-CR on HSE-2 cell viability. Cell viability of 100% corresponds with untreated cell MTT average reduction value, (**b**) Anti-inflammatory effect of different experimental groups on LPS-induced skin inflammation (NLRP3) level(I), IL-6(II), TNF-α(III), and IL-1β(IV).

Note: GO: graphene oxide, LPS: Lipopolysaccharide, CR: Cranberry powder, GO-CR: green graphene oxide nanosheet by using cranberry and PVA/CH/GO-CR hydrogel. Data are represented as mean± SEM (n = 6). P value *=0.0340, and ***=0.0001.

that there were no harmful effects of the green graphene oxide nanosheet by Cranberry employed in the hydrogel formulation.[27] Moreover, the PVA/CH/GO-CR hydrogel demonstrated a notable rise in flow when applied to cells, especially in reaction to stimuli like oxidative stress or acute inflammation. This implies that even under skin conditions that are compromised, the gel formulation may offer a prolonged release of proteins, increasing their bioavailability. These findings indicate the biocompatibility of the PVA/CH/GO-CR hydrogel when in contact with skin cells, as the formulation's components are usually regarded as safe.[1,27,67]

Effect of PVA/CH/GO-CR Treatment on Serum Inflammatory Cytokines Protein Profiles; Pyrin Domain-Containing Protein 3 (NLRP3), TNF-α, IL-1β, and IL-6

LPS-induced wound inflammation alters inflammatory cytokines. Previously, we discovered that applying PVA/CH/GO-CR hydrogel to wounds reduced LPS-induced levels of NLRP3, IL-6, IL-1β, and TNF-α in vitro. We obtained serum samples from rats three hours after administering LPS to assess the effects of PVA/CH/GO-CR hydrogel or cranberries on serum cytokine profiles. Compared to the control group, PVA/CH/GO-CR hydrogel therapy significantly reduced the expression of NLRP3, TNF-α, IL-6, and IL-1β (39.2%, 31.9%, 41%, and 52.3%, respectively) (Figure 9b). IL-1β, a key pro-inflammatory mediator in local acute inflammation, suggests that PVA/CH/GO-CR hydrogel therapy may be effective in treating wound inflammation. Numerous studies have indicated that immunoregulatory cytokines affect wound inflammation. TNF-α controls IL-6 levels in the early stages of inflammation. IL-1β, an alarm-phase cytokine, is linked to many wound-related symptoms.[28] TNF-α inhibition and increased IL-1β receptor antagonist levels are seen (Figure 9b). One major part of skin pathophysiology is inflammation. Skin tissue leakage induces adipose lipolysis, which releases damaging unsaturated fatty acids, including arachidonic acid, a precursor to pro-inflammatory eicosanoids. They release too many inflammatory markers, which can exacerbate the illness and create sores. The innate immune system promotes pathogenesis and illness. The innate immune receptor TLR4 detects pathogen- or damage-related molecular patterns. NLRP3, IL-6, TNF-α, and IL-1β suppression have been shown to reduce LPS-induced wound inflammation in previous studies. Our investigation demonstrated that a PVA/CH/GO-CR hydrogel treatment to Cranberry powder significantly reduced blood levels of NLRP3, IL-6, TNF-α, and IL-1β three hours after LPS injection. The increased wound healing benefits of PVA/CH/GO-CR hydrogel may be due to immunoregulatory cytokine regulation.[49]

In vivo Investigation

Because of the electroactive and photothermal antibacterial properties of graphene oxide, as well as the antimicrobial and anti-inflammatory properties of GO-CR, along with the antiulcer properties of cranberry and hydrogel, the use of PVA/CH/GO-CR hydrogel proved to be particularly helpful during the early phases of wound healing. By the third day of therapy, the animals receiving electroactive and photothermal treatment showed a notably higher percentage of wound healing than the other groups. On the other hand, the animal's recovery with the control drug progressed slowly. It was discovered that the cranberry concentration, more precisely, the electroactive and photothermal properties, was approximately 0.08%. This is based on the understanding that eco-friendly graphene oxide nanosheets frequently exhibit better bioavailability, enabling more potent therapeutic effects even at reduced dosages. Therefore, we administered a medication dosage at 1/10th of the standard dose and conducted a study, which yielded the following outcomes. By calculating the changes in wound area for each animal group, we determined the proportion of wound contraction. On the seventh and fourteenth days, significant wound contraction was observed, with daily observations tracking changes in the wound. Due to their innate immune responses, animals in group II showed only 15.5% healing, whereas group IV (the animals given GO-CR) demonstrated 89.21% healing. As observed in Figure 10 and Table 5, animals treated with Cranberry powder (group III) exhibited 41.4% healing, while those in the normal non-diabetic group (group I) showed 50.1% healing. By the seventh day, animals in group V demonstrated 92.9% healing, indicating complete recovery. Furthermore, images of wounds from group V, treated with PVA/CH/GO-CR hydrogel, also showed reduced wound diameters on the

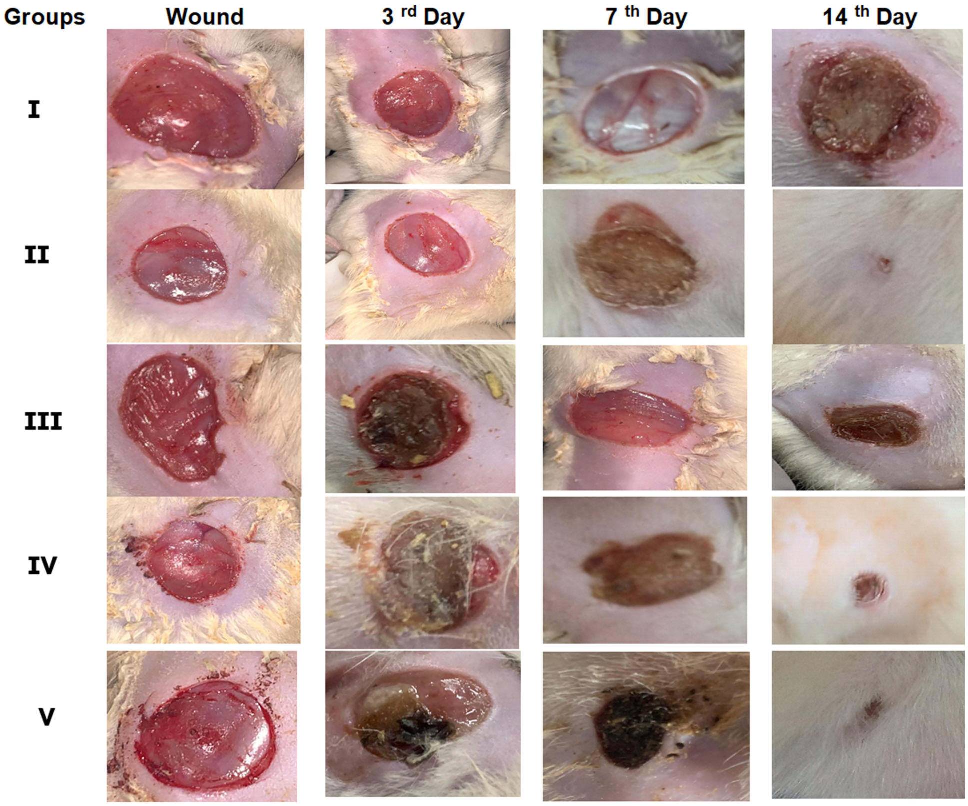

Figure 10 Comparison of the wound-healing activity of Group I (Diabetic untreated), Group II (diabetic treated by mebo and gentamycin), Group III (treated with Cranberry powder), and Group IV (treated with GO-CR) and Group V (PVA/CH/GO-CR hydrogel) at 3rd,7th and 14th day.

Table 5 Percentage of Wound-Healing Activity Against a Tested Sample of Groups

Group	Sample Name	Wound Concentration, % Mean ±S.D		
		3 rd	7 th	14th
I	**Diabetic**	9.5 ± 0.9	15.5 ± 0.5	30.3 ± 0.94
II	**Non-diabetic**	30.1 ± 0.6	50.1 ± 0.4	65.3 ± 0.5
III	**Cranberry**	25.1 ± 0.9	41.4 ± 0.6	50.5 ± 0.8
IV	**GO-CR**	54 ± 0.9	89.2 ± 0.5	90.2 ± 0.5
V	**PVA/CH/GO-CR hydrogel**	71.2 ± 0.8	92.1 ± 0.8	98.8 ± 0.7

seventh day. Cranberry shows promise in treating bacterial infections, ulcers, and inflammation related to wound healing. It contains compounds such as proanthocyanidins and organic acids with antimicrobial properties, inhibiting the growth of various bacteria commonly involved in skin infections like *E. coli*, and *Staphylococcus aureus*. Additionally, cranberry components like flavonoids and polyphenols possess anti-inflammatory properties, reducing the production of pro-inflammatory molecules in the body.[7] This anti-inflammatory effect aids in alleviating inflammation associated with wound healing and ulcer formation, promoting better healing outcomes. Moreover, cranberry contains compounds that promote wound healing by facilitating tissue repair and regeneration. These compounds reduce inflammation at the wound site, promote the proliferation of skin cells, and enhance collagen synthesis, crucial processes for effective wound healing. The antioxidants present in cranberries protect skin cells from oxidative damage induced by infection-induced inflammation and free radicals, supporting the healing process.[1,68] The reported anti-ulcer, urinary tract infection, and gastro-protective actions of Cranberry powder may be attributed to its active phytoconstituents, flavonoids, and phenolics. Graphene oxide nanosheets also possess anti-inflammatory, antibacterial, and wound-healing properties. The combination of CR powder extract, GO, and hydrogel significantly improved wound healing, consistent with previous investigations on Cranberry.[69,70]

Histopathological and Immunohistochemical (IHC) Examination of Vascular Endothelial Growth Factor (VEGF)

Figure11a–c. Photomicrographs of histological sections of skin from different experimental groups stained with Hematoxylin and Eosin (a) skin section on the 3rd day, (b) skin sections on the 7th day, and (c) skin sections on the 14thday Photomicrographs of H&E-stained skin sections from group I (3, 7, 14 days) diabetic untreated indicate increased wound area covered by big dried necrotic scabs underlined by diffusely necrotic and inflammatory tissue infiltrate (primarily neutrophils) with numerous extravasated RBCs (Figure11a–c I). Skin section of group II 3 days after wound induction showing abnormal epidermis with dried necrotic scab and underlying dermis of collagen and skin appendages with necrotic and inflammatory infiltrate (Figure 11a II). Skin sections of Cranberry powder (CR) (Group III) and green graphene oxide nanosheet (GO-CR) (group IV) 3 days after wound induction reveal identical lesions covered by necrotic scabs with less neutrophilic infiltration and less necrosis (Figure 11a III, IV). Skin sections of PVA/CH/GO-CR hydrogel (group V) treated 3 days after wound induction show a tiny dry necrotic scab (s) with less neutrophilic infiltration and less necrosis (Figure 11a V). Skin sections from the diabetic group 7 days after wound induction show increased wound area covered by contracted dry necrotic scab (s) emphasized by necrotic tissue and vascularized granulation tissue deposition with numerous macrophages and lymphocytes (Figure 11b II). Skin sections from the Cranberry-treated group (group III) 7 days after wound induction show dried necrotic scabs emphasized by tiny necrotic tissue infiltrated by neutrophils and vascularized granulation tissue deposition with macrophages and lymphocytic infiltration (Figure 11b III). Skin sections from the green graphene oxide nanosheet (GO-CR) (group IV) treated at 7 days after wound induction show disappeared dried necrotic scab with the newly separated epidermis (few squamous layers) underlined by very small necrotic tissue and vascularized granulation tissue deposition with many macrophages and lymphocytic infiltration (Figure 11b IV). Skin sections of PVA/CH/GO-CR hydrogel (group V) treated at 7 days after wound induction show disappeared dried necrotic scab, new epidermis (several keratinized ortho-epidermal layers), vascularized granulation

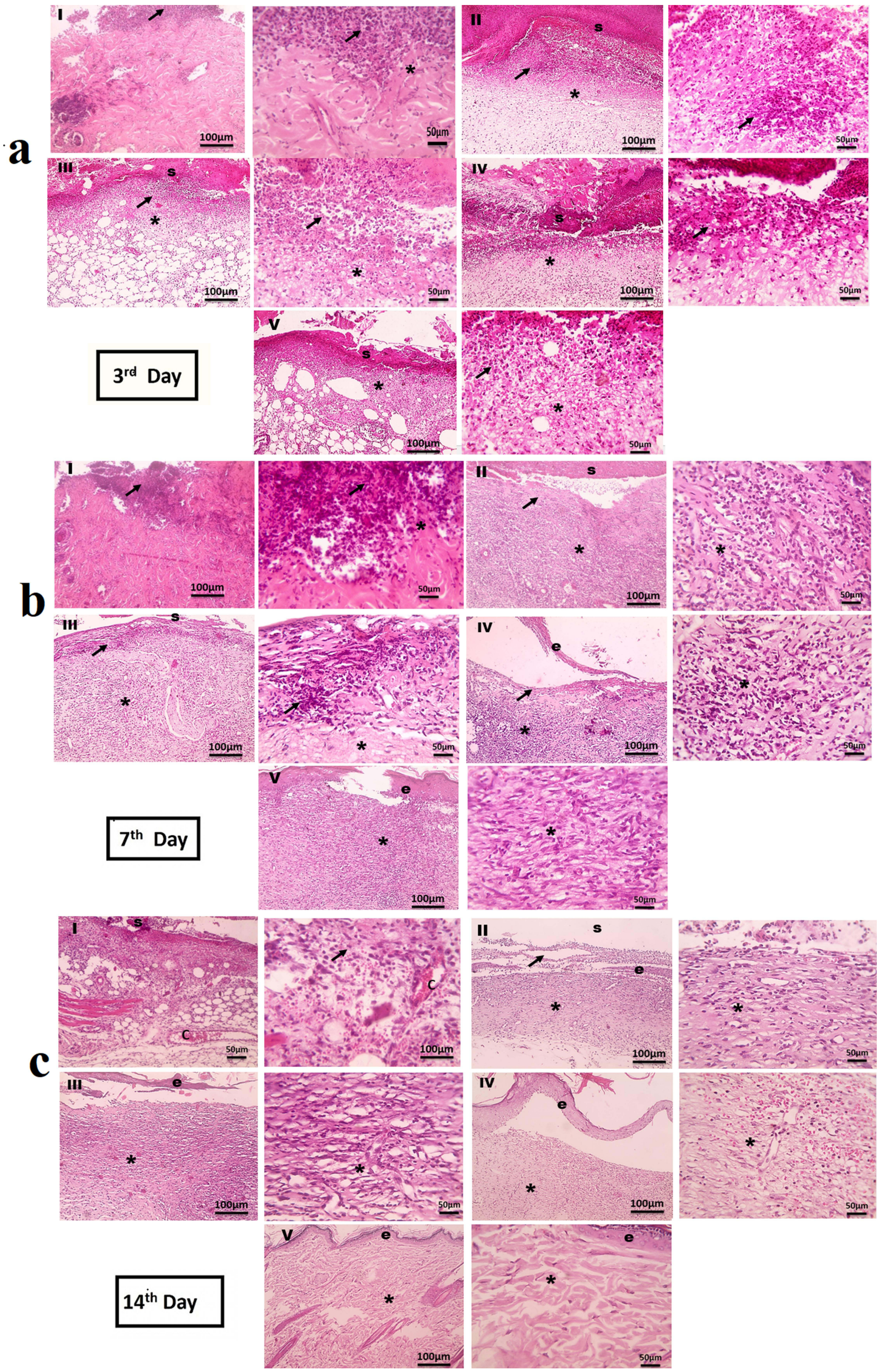

Figure 11 (a–c) Photomicrographs of histological sections of skin from different experimental groups stained with Hematoxylin and Eosin (**a**) skin section on the 3rd day, (**b**) skin sections on 7th day, and (c) skin sections on the 14th day. After wound induction group I with severe inflammatory cell infiltrate (thin black arrow) and necrotic area (*) and congested dilated blood vessel (**c**). Skin sections from Group II indicate increased wound area covered by big dried necrotic scab (s) underlined by diffusely necrotic (*) and inflammatory tissue infiltrate (primarily neutrophils) (black arrows) with numerous extravasated RBCs. Group III and Group IV skin sections reveal identical lesions covered by necrotic scab (s) with less neutrophilic infiltration (black arrows) and less necrosis (*). Skin sections from Group V show a tiny dry necrotic scab (s) less neutrophilic infiltration (thin black arrows) and less necrosis (*). Epidermis (e) with fully mature connective tissue replacing granulation tissue (*) with collagen and hair follicles. Low magnification ×100 bar 100 and high magnification x400 bar 50).

Note: Group I (diabetic non-treated), Group II (treated with ST), Group III (treated with Cranberry powder), Group IV (treated with GO-CR) and Group V (PVA/CH/GO-CR hydrogel).

tissue deposition, and few macrophages and lymphocytic infiltration (Figure 11b V). Skin sections from the Diabetic group 14 days after wound induction indicate increased wound area, dry necrotic scab disappearance, inflammatory exudate (black arrows), new epidermis, vascularized granulation tissue deposition with macrophages, and lymphocytic infiltration (Figure 11c II). Skin sections from the Cranberry-treated group (group III) treated at 14 days after wound induction indicate a newly divided epidermis (few keratinized epithelial layers) and vascularized granulation tissue deposition with macrophages and lymphocytic infiltration (Figure 11c III). Skin sections from the green graphene oxide nanosheet (GO-CR) (group IV) at 14 days after wound induction exhibiting newly divided epidermis (multiple keratinized epithelial layers) underlined by vascularized granulation tissue deposition containing few macrophages and lymphocytic infiltration (Figure 11c IV). Skin sections of PVA/CH/GO-CR hydrogel (group V) treated 14 days after wound induction demonstrate complete reepithelization with fully mature connective tissue, replacing granulation tissue with collagen and hair follicles (Figure 11c V).

Showing (I) few positively stained capillaries in the dermis (black arrows) without difference among 3-time points. (II) The immunostained skin sections against VGEF showed slightly increased numbers of positively stained capillaries in the wounded area 3 days after wound induction (black arrows) that moderately increased after 7 days and then decreased after 14 days. The immunostained skin sections against VGEF from treated groups (III, IV & V) showed higher numbers of positively stained capillaries in the wounded area 3 days after wound induction (black arrows) than in the (II), then decreased over time. IHC counterstained with Mayer's Hematoxylin. Magnification X: 400 bar 50.

Figure 12. Bars demonstrate numbers of VGEF-positive capillaries in immunostained skin samples from all groups by one-way ANOVA followed by Tukey's test to compare all means. Immunostained skin sections against VGEF showed

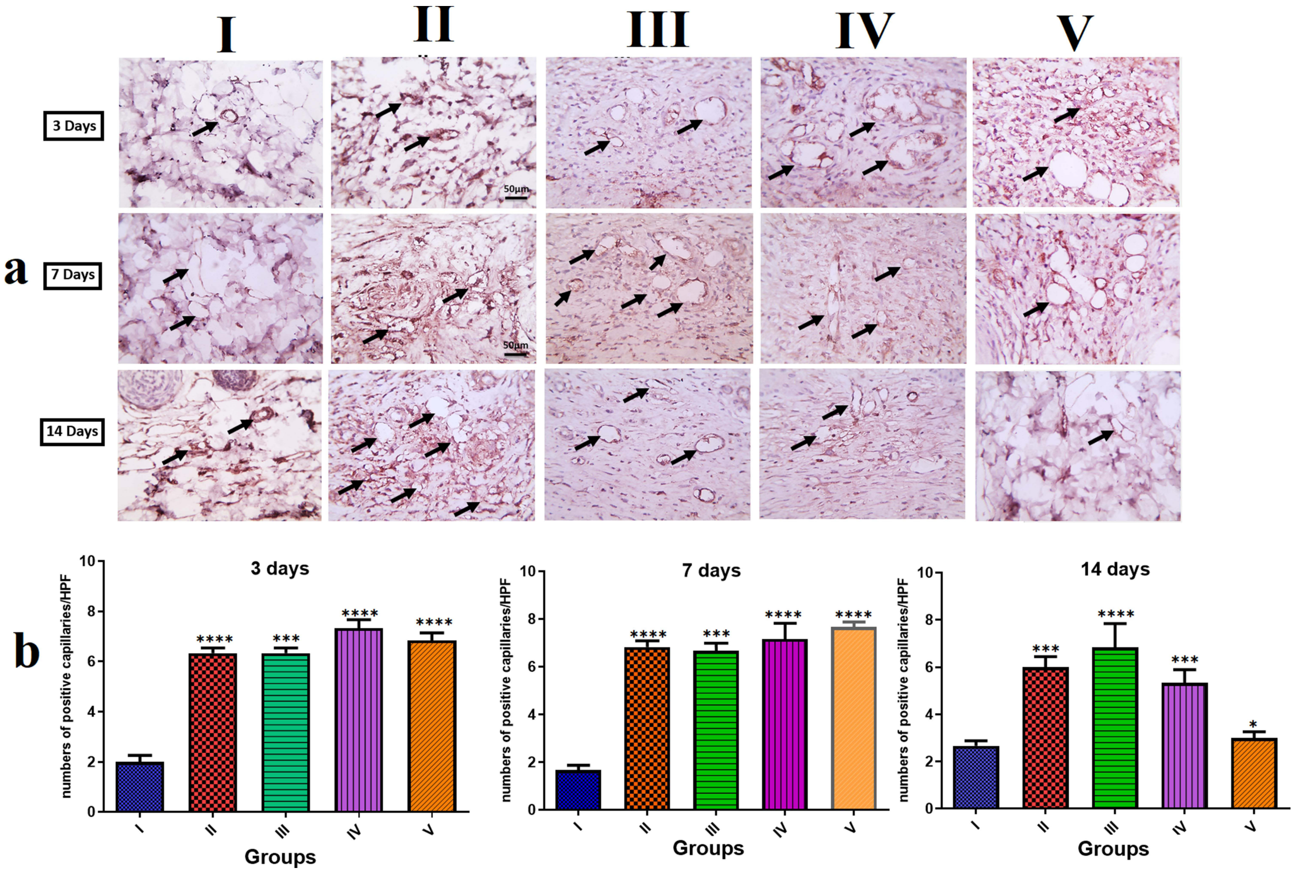

Figure 12 (a) Photomicrographs of immunostained skin sections against VGEF at 3 Days, 7 Days, and 14 Days after wound induction. (Magnification x400 bar 50).**(b)**. Bars demonstrate numbers of VGEF-positive capillaries in immunostained skin samples from all groups by one-way ANOVA followed by Tukey's test to compare all means.
Note: Black arrow Indicates the immunostained of VEGF in the wall of the blood vessels, P values *=0.0340, ***=0.0001, and ****<0.0001, and Group I (diabetic non-treated), group II (treated with ST), group III (treated with Cranberry powder), group IV (treated with GO-CR) and Group V (PVA/CH/GO-CR hydrogel.

few positively stained capillaries in the dermis without difference among 3-time points in the gp 1. The immunostained skin sections against VGEF from the gpI showed slightly increased numbers of positively stained capillaries in the wounded area 3 days after wound induction that moderately increased after 7 days and then decreased after 14 days. The immunostained skin sections against VGEF from treated groups showed higher numbers of positively stained capillaries in the wounded area 3 days after wound induction than in the gp1 then decreased by time.[71]

Conclusion

This study aimed to environmentally synthesize graphene oxide nanosheets (GO) using powdered cranberry extract, with the creation of PVA/CH/GO-CR hydrogel to facilitate wound healing. Gallic acid and Rosmarinic acid were identified as the predominant phenolic components in the cranberry extract. Through various analyses including FTIR, SEM, TEM, mechanical property, and electrical conductivity studies, we characterized the PVA/CH/GO-CR hydrogel. Antibacterial biofilm testing using the diffusion agar method revealed its efficacy against both Gram-positive (*Staphylococcus aureus* and *S. epidermidis*) and Gram-negative (*E. coli* and *Klebsiella pneumonia*) bacteria. Molecular dynamics and system stability in-silico studies were conducted to elucidate the chemical components involved in wound healing. The PVA/CH/GO-CR hydrogel exhibited superior anti-inflammatory effects, with reduced downregulation of NLRP3, IL-6, TNF-α, and IL-1β. Immunohistochemistry for vascular endothelial growth factor (VEGF), in vivo experiments, and histopathology analyses collectively supported the nanoparticles' ability to mitigate inflammation and expedite wound healing. Notably, in diabetic rats, the PVA/CH/GO-CR hydrogel demonstrated significant efficacy in wound healing, as evidenced by histological assessments and measurements of wound contraction.

Our findings underscore the potential of green-synthesized GO-CR nanosheets incorporated into PVA/CH hydrogel for drug delivery in wound healing applications, opening avenues for further research and development in this promising field.

Abbreviations

GO, Graphene Oxide; CR, Cranberry Extract; PVA, Polyvinyl Alcohol; CH, Chitosan; FTIR, Fourier Transform Infrared Spectroscopy; SEM, Scanning Electron Microscopy; TEM, Transmission Electron Microscopy; IL-6, Interleukin-6; TNF-α, Tumor Necrosis Factor-alpha; IL-1β, Interleukin-1 beta; VEGF, Vascular Endothelial Growth Factor; IHC, Immunohistochemical; H&E, Hematoxylin and Eosin (staining); ANOVA, Analysis of Variance; XRD, X-ray Diffraction; UV-Vis, Ultraviolet-Visible (spectroscopy); NLRP3, NOD-like Receptor Family Pyrin Domain Containing 3; DLS, Dynamic Light Scattering; ELISA, Enzyme-Linked Immunosorbent Assay; UV, Ultraviolet; MMPs, Matrix Metalloproteinases; HPLC, High-Performance Liquid Chromatography; MIC, Minimum Inhibitory Concentration; MBC, Minimum Bactericidal Concentration.

Data Sharing Statement

Data will be made available on request.

Author Contributions

All authors made a significant contribution to the work reported, whether that is in the conception, study design, execution, acquisition of data, analysis and interpretation, or all these areas; took part in drafting, revising or critically reviewing the article; gave final approval of the version to be published; have agreed on the journal to which the article has been submitted; and agree to be accountable for all aspects of the work.

Funding

This work was partially funded by the University of Sharjah for AA.

Disclosure

The authors declare that they have no known competing financial interests or personal relationships that could have appeared to influence the work reported in this paper.

References

1. Elhabal S, Abdelaal N, Saeed Al-Zuhairy S, et al. Green Synthesis of Zinc Oxide Nanoparticles from Althaea Officinalis Flower Extract Coated with Chitosan for Potential Healing Effects on Diabetic Wounds by Inhibiting TNF-α and IL-6/IL-1β Signaling Pathways. *Int J Nanomed*. 2024;19:3045–3070. doi:10.2147/IJN.S455270
2. Oprita EI, Iosageanu A, Craciunescu O. Natural Polymeric Hydrogels Encapsulating Small Molecules for Diabetic Wound Healing. *Gels*. 2023;9. doi:10.3390/gels9110867
3. Agyare C, Boakye YD, Bekoe EO, Hensel A, Dapaah SO, Appiah T. Review: African Medicinal Plants with Wound Healing Properties. *J Ethnopharmacol*. 2016;177:85–100. doi:10.1016/j.jep.2015.11.008
4. Fathy Elhabal S, El-Nabarawi MA, Abdelaal N, et al. Development of Canagliflozin Nanocrystals Sublingual Tablets in the Presence of Sodium Caprate Permeability Enhancer: formulation Optimization, Characterization, in-Vitro, in Silico, and in-Vivo Study. *Drug Deliv*. 2023;30. doi:10.1080/10717544.2023.2241665
5. Teaima MH, Badawi NM, Attia DA, El-Nabarawi MA, Elmazar MM, Mousa SA. Efficacy of Pomegranate Extract Loaded Solid Lipid Nanoparticles Transdermal Emulgel against Ehrlich Ascites Carcinoma. *Nanomedicine*. 2022;39. doi:10.1016/J.NANO.2021.102466
6. Brown PN, Turi CE, Shipley PR, Murch SJ. Comparisons of Large (Vaccinium Macrocarpon Ait.) and Small (Vaccinium Oxycoccos L, Vaccinium Vitis-Idaea L.) Cranberry in British Columbia by Phytochemical Determination, Antioxidant Potential, and Metabolomic Profiling with Chemometric Analysis. *Planta Med*. 2012;78:630–640. doi:10.1055/S-0031-1298239
7. Poljšak N, Kreft S, Kočevar Glavač N. Vegetable Butters and Oils in Skin Wound Healing: scientific Evidence for New Opportunities in Dermatology. *Phytother Res*. 2020;34:254–269. doi:10.1002/PTR.6524
8. El-Nawawy TM, Adel YA, Teaima M, et al. Intranasal bilosomes in thermosensitive hydrogel: advancing desvenlafaxine succinate delivery for depression management. *Pharm Dev Technol*. 2024;29(7):663–674. doi:10.1080/10837450.2024.2376067
9. Wojnicz D, Tichaczek-Goska D, Korzekwa K, Kicia M, Hendrich AB. Study of the Impact of Cranberry Extract on the Virulence Factors and Biofilm Formation by Enterococcus Faecalis Strains Isolated from Urinary Tract Infections. *Int J Food Sci Nutr*. 2016;67:1005–1016. doi:10.1080/09637486.2016.1211996
10. Thakur S, Anjum MM, Jaiswal S, et al. Novel Synergistic Approach: tazarotene-Calcipotriol-Loaded-PVA/PVP-Nanofibers Incorporated in Hydrogel Film for Management and Treatment of Psoriasis. *Mol Pharm*. 2023;20:997–1014. doi:10.1021/acs.molpharmaceut.2c00713
11. Liu Y, Mao J, Guo Z, Hu Y, Wang S. Polyvinyl Alcohol/Carboxymethyl Chitosan Hydrogel Loaded with Silver Nanoparticles Exhibited Antibacterial and Self-Healing Properties. *Int J Biol Macromol*. 2022;220:211–222. doi:10.1016/J.IJBIOMAC.2022.08.061
12. Adhikari HS, Garai A, Manandhar KD, Yadav PN. Pyridine-Based NNS Tridentate Chitosan Thiosemicarbazones and Their Copper(II) Complexes: synthesis, Characterization, and Anticancer Activity. *ACS Omega*. 2022;7:30978–30988. doi:10.1021/ACSOMEGA.2C02966/ASSET/IMAGES/LARGE/AO2C02966_0003.JPEG
13. Teaima MH, Elasaly MK, Omar SA, El-Nabarawi MA, Shoueir KR. Eco-Friendly Synthesis of Functionalized Chitosan-Based Nanoantibiotic System for Potential Delivery of Linezolid as Antimicrobial Agents. *Saudi Pharm J*. 2020;28:859–868. doi:10.1016/J.JSPS.2020.06.005
14. Yasser M, El Naggar EE, Elfar N, Teaima MH, El-Nabarawi MA, Elhabal SF. Formulation, Optimization and Evaluation of Ocular Gel Containing Nebivolol Hcl-Loaded Ultradeformable Spanlastics Nanovesicles: in Vitro and in Vivo Studies. *Int J Pharm X*. 2024;7. doi:10.1016/J.IJPX.2023.100228
15. Fouad SA, Teaima MH, Gebril MI, Abd Allah FI, El-Nabarawi MA, Elhabal SF. Formulation of Novel Niosomal Repaglinide Chewable Tablets Using Coprocessed Excipients: in Vitro Characterization, Optimization and Enhanced Hypoglycemic Activity in Rats. *Drug Deliv*. 2023;30. doi:10.1080/10717544.2023.2181747
16. Yan H, Li P, Jiang X, et al. Preparation of Graphene Oxide/Polydopamine-Curcumin Composite Nanomaterials and Its Antibacterial Effect against Staphylococcus Aureus Induced by White Light. *Biomaterials Advances*. 2022;139. doi:10.1016/J.BIOADV.2022.213040
17. Kondo S, Nishimura T, Nishina Y, Sano K. Countercation Engineering of Graphene-Oxide Nanosheets for Imparting a Thermoresponsive Ability. *ACS Appl Mater Interfaces*. 2023;15:37837–37844. doi:10.1021/ACSAMI.3C07820
18. ELhabal SF, El-Nabarawi MA, Hassanin SO, et al. Transdermal fluocinolone acetonide loaded decorated hyalurosomes cellulose acetate/polycaprolactone nanofibers mitigated Freund's adjuvant-induced rheumatoid arthritis in rats. *J Pharm Investig*. 2004. doi: 10.1007/s40005-024-00693-8
19. Odjo K, Al-Maqtari QA, Yu H, et al. Preparation and Characterization of Chitosan-Based Antimicrobial Films Containing Encapsulated Lemon Essential Oil by Ionic Gelation and Cranberry Juice. *Food Chem*. 2022;397. doi:10.1016/j.foodchem.2022.133781
20. Alfaro-Viquez E, Esquivel-Alvarado D, Madrigal-Carballo S, Krueger CG, Reed JD. Antimicrobial Proanthocyanidin-Chitosan Composite Nanoparticles Loaded with Gentamicin. *Int J Biol Macromol*. 2020;162:1500–1508. doi:10.1016/j.ijbiomac.2020.07.213
21. Lozano-Navarro JI, Díaz-Zavala NP, Velasco-Santos C, et al. Chitosan-Starch Films with Natural Extracts: physical, Chemical, Morphological and Thermal Properties. *Materials*. 2018;11. doi:10.3390/ma11010120
22. Cao J, He G, Ning X, et al. Preparation and Properties of O-Chitosan Quaternary Ammonium Salt/Polyvinyl Alcohol/Graphene Oxide Dual Self-Healing Hydrogel. *Carbohydr Polym*. 2022;287. doi:10.1016/J.CARBPOL.2022.119318
23. Shoman NA, Saady M, Teaima M, Abdelmonem R, El-Nabarawi MA, Elhabal SF. Merging Konjac Glucomannan with Other Copolymeric Hydrogels as a Cutting-Edge Liquid Raft System for Dual Delivery of Etoricoxib and Famotidine. *Drug Deliv*. 2023;30. doi:10.1080/10717544.2023.2189630
24. Abdelmonem R, Elhabal SF, Abdelmalak NS, El-Nabarawi MA, Teaima MH. Formulation and Characterization of Acetazolamide/Carvedilol Niosomal Gel for Glaucoma Treatment: in Vitro, and In Vivo Study. *Pharmaceutics*. 2021;13:1–20. doi:10.3390/PHARMACEUTICS13020221
25. Abd-Elrahman AA, El Nabarawi MA, Hassan DH, Taha AA. Ketoprofen Mesoporous Silica Nanoparticles SBA-15 Hard Gelatin Capsules: preparation and in Vitro/in Vivo Characterization. *Drug Deliv*. 2016;23:3387–3398. doi:10.1080/10717544.2016.1186251
26. El-Nabarawi MA, Ali AA, Aboud HM, Hassan AH, Godah AH. Transbuccal Delivery of Betahistine Dihydrochloride from Mucoadhesive Tablets with a Unidirectional Drug Flow: in Vitro, Ex Vivo and in Vivo Evaluation. *Drug Des Devel Ther*. 2016;10:4031–4045. doi:10.2147/DDDT.S120613

27. Hamza AA, Khasawneh MA, Elwy HM, Hassanin SO, Elhabal SF, Fawzi NM. Salvadora Persica Attenuates DMBA-Induced Mammary Cancer through Downregulation Oxidative Stress, Estrogen Receptor Expression and Proliferation and Augmenting Apoptosis. *Biomed. Pharmacother*. 2022;147:112666. doi:10.1016/J.BIOPHA.2022.112666
28. Abdelfattah DSE, Fouad MA, Elmeshad AN, El-Nabarawi MA, Elhabal SF. Anti-Obesity Effect of Combining White Kidney Bean Extract, Propolis Ethanolic Extract and CrPi3 on Sprague-Dawley Rats Fed a High-Fat Diet. *Nutrients*. 2024;16:310. doi:10.3390/NU16020310
29. Elhabal SF, Abdelmonem R, El Nashar RM, et al. Enhanced Antibacterial Activity of Clindamycin Using Molecularly Imprinted Polymer Nanoparticles Loaded with Polyurethane Nanofibrous Scaffolds for the Treatment of Acne Vulgaris. *Pharmaceutics*. 2024;16(947). doi:10.3390/PHARMACEUTICS16070947
30. Matica MA, Aachmann FL, Tøndervik A, Sletta H, Ostafe V. Chitosan as a Wound Dressing Starting Material: antimicrobial Properties and Mode of Action. *Int J Mol Sci*. 2019;20. doi:10.3390/IJMS20235889
31. Di Giulio M, Zappacosta R, Di Lodovico S, et al. Antimicrobial and Antibiofilm Efficacy of Graphene Oxide against Chronic Wound Microorganisms. *Antimicrob Agents Chemother*. 2018;62. doi:10.1128/AAC.00547-18
32. Mohammed MHH, Hamed ANE, Elhabal SF, et al. Metabolic Profiling and Cytotoxic Activities of Ethanol Extract of Dypsis Leptocheilos Aerial Parts and Its Green Synthesized Silver Nanoparticles Supported by Network Pharmacology Analysis. *S Afr J Bot*. 2023;161:648–665. doi:10.1016/J.SAJB.2023.08.026
33. Fathy Elhabal S, El-Nabarawi MA, Abdelaal N, et al. Development of Canagliflozin Nanocrystals Sublingual Tablets in the Presence of Sodium Caprate Permeability Enhancer: formulation Optimization, Characterization, in-Vitro, in Silico, and in-Vivo Study. *Drug Deliv*. 2023;30:2241665. doi:10.1080/10717544.2023.2241665
34. Hanwell MD, Curtis DE, Lonie DC, Vandermeerschd T, Zurek E, Hutchison GR. Avogadro: an Advanced Semantic Chemical Editor, Visualization, and Analysis Platform. *J Cheminform*. 2012;4. doi:10.1186/1758-2946-4-17
35. Mason AC, Jensen JH. Protein-Protein Binding Is Often Associated with Changes in Protonation State. *Proteins*. 2008;71:81–91. doi:10.1002/prot.21657
36. Filipe HAL, Loura LMS. Molecular Dynamics Simulations: advances and Applications. *Molecules*. 2022;27. doi:10.3390/MOLECULES27072105
37. Moffett AS, Shukla D. Using Molecular Simulation to Explore the Nanoscale Dynamics of the Plant Kinome. *Biochem. J*. 2018;475:905–921. doi:10.1042/BCJ20170299
38. Roy P, Walter Z, Berish L, Ramage H, McCullagh M. Motif-VI Loop Acts as a Nucleotide Valve in the West Nile Virus NS3 Helicase. *bioRxiv*. 2023. doi:10.1101/2023.11.30.569434
39. Roe DR, Cheatham TE. PTRAJ and CPPTRAJ: software for Processing and Analysis of Molecular Dynamics Trajectory Data. *J Chem Theory Comput*. 2013;9:3084–3095. doi:10.1021/CT400341P
40. Mahdizadeh SJ, Stier M, Carlesso A, Lamy A, Thomas M, Eriksson LA. Multiscale In Silico Study of the Mechanism of Activation of the RtcB Ligase by the PTP1B Phosphatase. *J Chem Inf Model*. 2023. doi:10.1021/acs.jcim.3c01600
41. Pettersen EF, Goddard TD, Huang CC, et al. UCSF Chimera–a Visualization System for Exploratory Research and Analysis. *J Comput Chem*. 2004;25:1605–1612. doi:10.1002/JCC.20084
42. Kollman PA, Massova I, Reyes C, et al. Calculating Structures and Free Energies of Complex Molecules: combining Molecular Mechanics and Continuum Models. *Acc Chem Res*. 2000;33:889–897. doi:10.1021/AR000033J
43. Ylilauri M, Pentikäinen OT. MMGBSA as a Tool to Understand the Binding Affinities of Filamin-Peptide Interactions. *J Chem Inf Model*. 2013;53:2626–2633. doi:10.1021/CI4002475
44. Elhabal SF, Teaima MH, Shawqiali Y, El-Nabarawi MA, Abdelmonem R, Elfar N. TASTE MASKED CLOPERASTINE HYDROCHLORIDE AND RUPATADINE ORAL DISPERSIBLE TABLETS: FORMULATION DESIGN, DEVELOPMENT, CHARACTERIZATION AND PHARMACOKINETICS STUDY ON WISTAR RATS. *Int J Appl Pharm*. 2023;15:191–200. doi:10.22159/IJAP.2023V15I4.47824
45. Mohammed MHH, Hamed ANE, Elhabal SF, et al. Chemical Composition and Anti-Proliferative Activities of Hyophorbe Lagenicaulis Aerial Parts and Their Biogenic Nanoparticles Supported by Network Pharmacology Study. *S Afr J Bot*. 2023;156:398–410. doi:10.1016/J.SAJB.2023.03.018
46. Elhabal SF, Elwy HM, Hassanin S, El-Rashedy AA, Hamza AA, Khasawneh MA. Biosynthesis and Characterization of Gold and Copper Nanoparticles from Salvadora Persica Fruit Extracts and Their Biological Properties. *Int J Nanomed*. 2022;17:6095. doi:10.1080/10837450.2024.2376067
47. Tietel Z, Melamed S, Ogen-Shtern N, et al. Topical Application of Jojoba (Simmondsia Chinensis L.) Wax Enhances the Synthesis of pro-Collagen III and Hyaluronic Acid and Reduces Inflammation in the Ex-Vivo Human Skin Organ Culture Model. *Front Pharmacol*. 2024;15:1333085. doi:10.3389/fphar.2024.1333085
48. Liu Z, Wang Y, Ning Q, et al. The Role of Spleen in the Treatment of Experimental Lipopolysaccharide-Induced Sepsis with Dexmedetomidine. *Springerplus*. 2015;4:1–7. doi:10.1186/S40064-015-1598-Y
49. Elhabal SF, Abdelaal N, Al-Zuhairy SAS, et al. Revolutionizing Psoriasis Topical Treatment: enhanced Efficacy Through Ceramide/Phospholipid Composite Cerosomes Co-Delivery of Cyclosporine and Dithranol: in-Vitro, Ex-Vivo, and in-Vivo Studies. *Int J Nanomed*. 2024;19:1163–1187. doi:10.2147/IJN.S443812
50. Al-Shoubki AA, Teaima MH, Abdelmonem R, El-Nabarawi MA, Elhabal SF. Sucrose Acetate Isobutyrate (SAIB) and Glyceryl Monooleate (GMO) Hybrid Nanoparticles for Bioavailability Enhancement of Rivaroxaban: an Optimization Study. *Pharm Dev Technol*. 2023;28:928–938. doi:10.1080/10837450.2023.2274944
51. Aly AA, Ahmed MK. Nanofibers of Cellulose Acetate Containing ZnO Nanoparticles/Graphene Oxide for Wound Healing Applications. *Int J Pharm*. 2021;598. doi:10.1016/J.PSCIA.2023.100015
52. Fang Z, Chen H, Wei Y-Q, et al. Bioelectricity and CO2-to-Butyrate Production Using Photobioelectrochemical Cells with Bio-Hydrogel. *Bioresour Technol*. 2024;398:130530. doi:10.1016/j.biortech.2024.130530
53. Pei S, Wei Q, Huang K, Cheng HM, Ren W. Green Synthesis of Graphene Oxide by Seconds Timescale Water Electrolytic Oxidation. *Nat Commun*. 2018;9. doi:10.1038/S41467-017-02479-Z
54. Ramezanzadeh M, Bahlakeh G, Ramezanzadeh B. Construction of an Epoxy Composite with Excellent Thermal/Mechanical Properties Using Graphene Oxide Nanosheets Reduced/Functionalized by *Tamarindus indiaca* Extract/Zinc Ions; Detailed Experimental and DFT-D Computer Modeling Explorations. *Results Phys*. 2020;19:103400. doi:10.1016/J.RINP.2020.103400

55. Chaudhary JP, Kholiya F, Vadodariya N, Budheliya VM, Gogda A, Meena R. Carboxymethylagarose-Based Multifunctional Hydrogel with Super Stretchable, Self-Healable Having Film and Fiber Forming Properties. *Arabian J Chem*. 2020;13:1661–1668. doi:10.1016/j.arabjc.2017.12.034
56. El-Gizawy SA, Osman MA, Ibrahim SF. Effect of Cosolvents on the Absorptive Clearance of Ketotifen Fumarate from Rabbit Intestine, In-Situ. *J Adva Phar Res*. 2018;2:168–179. doi:10.21608/APRH.2018.3450.1055
57. Tantiwatcharothai S, Prachayawarakorn J. Property Improvement of Antibacterial Wound Dressing from Basil Seed (O. Basilicum L.) Mucilage-ZnO Nanocomposite by Borax Crosslinking. *Carbohydr Polym*. 2020;227. doi:10.1016/J.CARBPOL.2019.115360
58. Ewedah TM, Abdalla A, Hagag RS, et al. Enhancing Cellular Affinity for Skin Disorders: electrospun Polyurethane/Collagen Nanofiber Mats Coated with Phytoceramides. *Int J Pharm*. 2024;663:124541. doi:10.1016/J.IJPHARM.2024.124541
59. Barbosa F, Garrudo FFF, Marques AC, et al. Novel Electroactive Mineralized Polyacrylonitrile/PEDOT:PSS Electrospun Nanofibers for Bone Repair Applications. *Int J Mol Sci*. 2023;24. doi:10.3390/IJMS241713203
60. Al-Shoubki AA, Teaima MH, Abdelmonem R, El-Nabarawi MA, Elhabal SF. Potential Application of Sucrose Acetate Isobutyrate, and Glyceryl Monooleate for Nanonization and Bioavailability Enhancement of Rivaroxaban Tablets. *Pharmaceutical Science Advances*. 2024;2:100015. doi:10.1016/j.pscia.2023.100015
61. Giorda CB, Picariello R, Tartaglino B, et al. Hospitalisation for Herpes Zoster in People with and without Diabetes: a 10-Year-Observational Study. *Diabet Res Clin Pract*. 2024;111603. doi:10.1016/j.diabres.2024.111603
62. Wu G, Jin K, Liu L, Zhang H. A Rapid Self-Healing Hydrogel Based on PVA and Sodium Alginate with Conductive and Cold-Resistant Properties. *Soft Matter*. 2020;16:3319–3324. doi:10.1039/C9SM02455G
63. Li L, Mai Y, Wang Y, Chen S. Stretchable Unidirectional Liquid-Transporting Membrane with Antibacterial and Biocompatible Features Based on Chitosan Derivative and Composite Nanofibers. *Carbohydr Polym*. 2022;276. doi:10.1016/J.CARBPOL.2021.118703
64. Almutairi B, Albahser G, Almeer R, et al. Investigation of Cytotoxicity Apoptotic and Inflammatory Responses of Biosynthesized Zinc Oxide Nanoparticles from Ocimum Sanctum Linn in Human Skin Keratinocyte (Hacat) and Human Lung Epithelial (A549) Cells. *Oxid Med Cell Longev*. 2020;2020. doi:10.1155/2020/1835475
65. Shokri D, Khorasgani MR, Mohkam M, Fatemi SM, Ghasemi Y, Taheri-Kafrani A. The Inhibition Effect of Lactobacilli Against Growth and Biofilm Formation of Pseudomonas Aeruginosa. *Probiotics Antimicrob Proteins*. 2018;10:34–42. doi:10.1007/s12602-017-9267-9
66. Fouad SA, Malaak FA, Teaima MH, et al. Novel Inhalable Nano-Based/Microparticles for Enhanced Sustained Pulmonary Delivery of Remdesivir - A Patient Malleable Treatment for Coronaviruses Infection: in Vitro Aerosolization, Cytotoxicity Assays and Antiviral Activity Studies. *J Drug Deliv Sci Technol*. 2024;101. doi:10.1016/j.jddst.2024.106196
67. Al-Shoubki AA, Hassan M, Teaima M, et al. Bioavailability Enhancement Strategies for Rivaroxaban: a Noteworthy Review. *Article in Int J App Pharm*. 2023. doi:10.22159/ijap.2023v15i6.48839
68. Esposito D, Overall J, Grace MH, Komarnytsky S, Lila MA. Alaskan Berry Extracts Promote Dermal Wound Repair Through Modulation of Bioenergetics and Integrin Signaling. *Front Pharmacol*. 2019;10:1058. doi:10.3389/fphar.2019.01058
69. Šedbarė R, Janulis V, Ramanauskiene K. Formulation and Biopharmaceutical Evaluation of Capsules Containing Freeze-Dried Cranberry Fruit Powder. *Plants*. 2023;12. doi:10.3390/plants12061397
70. Šedbarė R, Janulis V, Ramanauskiene K. Edible Gels with Cranberry Extract: evaluation of Anthocyanin Release Kinetics. *Gels*. 2023;9. doi:10.3390/gels9100796
71. Eroglu ZT, Kurtis B, Altug HA, Sahin S, Tuter G, Baris E. Effect of Topical Ozonetherapy on Gingival Wound Healing in Pigs: histological and Immuno-Histochemical Analysis. *J Appl Oral Sci*. 2018;27. doi:10.1590/1678-7757-2018-0015